Ceramics International xxx (xxxx) xxx

Contents lists available at ScienceDirect

Ceramics International

journal homepage: www.elsevier.com/locate/ceramint

Densification and property optimization of $BaTiO_3$ piezoelectric ceramics fabricated by digital light processing with sintering aids

Yaxiang Sun [a], Peipei Wang [a], Weikai Shi [b], Xin Lan [a,*], Yanju Liu [b,c,**], Jinsong Leng [a]

[a] Center for Composite Materials and Structures, Harbin Institute of Technology, Harbin, 150080, People's Republic of China
[b] Department of Aerospace Engineering and Mechanics, Harbin Institute of Technology, Harbin, 150001, People's Republic of China
[c] Suzhou Research Institute, Harbin Institute of Technology, Suzhou, 215100, People's Republic of China

ARTICLE INFO

Keywords:
$BaTiO_3$
DLP 3D printing
Sintering aids
Wide-temperature-range sintering
Performance optimization

ABSTRACT

$BaTiO_3$ ceramics fabricated by conventional methods have been the primary focus of previous investigations. In contrast, the effects of different sintering aids on DLP-fabricated $BaTiO_3$ ceramics were systematically investigated over a wide sintering-temperature range. A DLP fabrication route incorporating sintering aids was employed to overcome the limitations of conventional fabrication in producing complex-structured lead-free piezoelectric ceramics with tailored properties. $BaTiO_3$ ceramics were fabricated using a high-solid-loading photosensitive slurry (85 wt%). Four independent compositions were prepared, each containing a single sintering aid (CuO, SiO_2, TEOS, or Li_2CO_3). The printed samples were subsequently sintered at temperatures ranging from 1375 to 1475 °C to establish clear processing–structure–property relationships. The results show that all sintering aids significantly influence densification behavior, microstructural evolution, and functional properties. Among them, TEOS-containing ceramics exhibit the most balanced overall performance, with optimal properties achieved within 1425–1450 °C. The sample sintered at 1425 °C shows the highest relative density (0.941) and dielectric constant (1904), while the maximum piezoelectric coefficient (d_{33} = 234 pC/N) is obtained at 1450 °C. CuO addition leads to the highest piezoelectric response (d_{33} = 258.7 pC/N), but is accompanied by abnormal grain growth and reduced microstructural stability. In contrast, SiO_2- and Li_2CO_3-containing samples exhibit comparatively lower overall performance due to less effective densification and microstructural development. Overall, a systematic comparative framework was established for evaluating the effects of different sintering aids on DLP-fabricated $BaTiO_3$ ceramics. The combination of sintering-aid engineering and additive manufacturing offers an effective route for optimizing the microstructure and multifunctional performance of lead-free piezoelectric ceramics for energy harvesting and sensing applications.

1. Introduction

Piezoelectric ceramics, owing to their outstanding electromechanical conversion capability, have been employed in porous functional structures and electromechanical energy-conversion devices [1,2]. Among them, barium titanate ($BaTiO_3$), as a representative lead-free perovskite ferroelectric ceramic, has attracted sustained attention because of its favorable dielectric, ferroelectric, and piezoelectric properties, which can be regulated through additive incorporation, powder characteristics, and sintering conditions [3–5]. Additively manufactured piezoelectric elements have also demonstrated potential for ultrasonic sensing and energy focusing [6]. Moreover, chemical substitution and sintering temperature strongly affect the phase composition, dielectric response, and ferroelectric properties of $BaTiO_3$-based ceramics [7,8]. The piezoelectric characteristics and biomedical application prospects of $BaTiO_3$ nanoparticles have also been reviewed [9]. Previous investigations have addressed electrocaloric behavior [10], modification of electrical properties by AlN and SiO_2 [11], the incorporation of $BaTiO_3$ into microwave dielectric glass-ceramics [12], two-step sintering strategies for ceramics [13], and high-permittivity $BaTiO_3$ fabrication routes [14]. In recent years, increasing efforts have therefore been devoted to improving the functional performance of $BaTiO_3$-based ceramics through microstructure engineering and advanced fabrication strategies.

* Corresponding author.
** Corresponding author. Department of Aerospace Engineering and Mechanics, Harbin Institute of Technology, Harbin, 150001, People's Republic of China.
E-mail addresses: lanxin@hit.edu.cn (X. Lan), yj_liu@hit.edu.cn (Y. Liu).

https://doi.org/10.1016/j.ceramint.2026.07.542
Received 27 April 2026; Received in revised form 29 July 2026; Accepted 30 July 2026
Available online 30 July 2026

However, conventional forming techniques are generally more suitable for ceramic components with relatively simple geometries and therefore impose limitations on the direct fabrication of intricate three-dimensional piezoelectric structures. Traditional methods such as dry pressing and tape casting provide limited geometric flexibility, whereas subsequent machining, although allowing shape modification, increases processing complexity and may adversely affect the surface integrity of brittle ceramic components. These limitations have motivated the development of additive manufacturing techniques for complex ceramic architectures.

The emergence of digital light processing (DLP) additive manufacturing [15,16] provides a promising route to overcome these limitations [17]. Recent reviews have highlighted that photopolymerization-based ceramic additive manufacturing enables the fabrication of complex ceramic architectures with high dimensional accuracy, while challenges associated with slurry stability, debinding defects, and densification control remain to be addressed [15,18]. Based on the mask-projection principle, DLP [4,19] enables the rapid fabrication of ceramic components with high dimensional accuracy [20] and complex geometries [1,4,21]. $BaTiO_3$ piezoelectric ceramics for focused ultrasonic arrays have been fabricated using photopolymerization-based approaches [22]. Advances in formulation-driven DLP processing and high-precision vat photopolymerization have also been reported [16,23,24]. In addition to improving printing accuracy and densification, compositional modification has recently been employed to enhance the functional performance of printed $BaTiO_3$-based ceramics. For example, high piezoelectricity was achieved in $BaTiO_3$–$BaSnO_3$ ceramics fabricated by vat photopolymerization, demonstrating that material composition can be combined with additive manufacturing to regulate phase-transition behavior and piezoelectric response [25]. Moreover, recent progress in vat photopolymerization technologies has further demonstrated their capability for manufacturing multifunctional ceramic components with tailored architectures and improved functional integration [26]. However, the removal of organic binders and the associated pore evolution during debinding and sintering remain important factors affecting final density and electrical performance. The final properties of photocured 3D-printed ceramics strongly depend on densification and microstructural evolution during sintering [18,24,27]. Previous reports have shown that the organic constituents in printed green bodies may lead to nonuniform shrinkage and residual porosity during debinding and sintering, thereby compromising mechanical and electrical performance [15,18,23].

The incorporation of additives and the control of sintering conditions [5,8,28,29] have been widely employed to regulate the densification and functional properties of $BaTiO_3$-based ceramics. In recent years, sintering-aid engineering has been increasingly explored as an approach for regulating grain-boundary transport, densification, and microstructural evolution in $BaTiO_3$-based ceramics. Appropriate composition and sintering control [30,31] can influence grain-growth behavior and densification [8,29–31], thereby modifying the dielectric and ferroelectric properties of $BaTiO_3$-based ceramics [8,10,28]. A variety of additive systems [11,28,32,33] have been investigated for $BaTiO_3$-based ceramics, including rare-earth dopants, oxide additives, lithium-containing compounds, and silicate- or glass-forming additives [5,11,32,33]. Systematic screening of sintering aids has also been reported for other oxide ceramic systems [34]. Among the additive systems considered here, SiO_2-containing and lithium-containing additives have been reported to influence densification, electrical properties, and grain-boundary-related processes [5,11,33,35], whereas CuO and TEOS have not yet been systematically compared under identical DLP processing conditions. These effects depend strongly on additive chemistry and processing conditions.

However, previous investigations have largely been limited to individual compositions or additive systems processed by conventional ceramic routes, whereas systematic investigations under photocuring-based additive-manufacturing conditions remain scarce. More importantly, investigations of the influence of sintering temperature on the density, shrinkage, and functional properties of $BaTiO_3$-based ceramics have generally been limited to individual material systems or comparatively narrow processing windows [3–5,7,33,36–38]. Accordingly, systematic comparative studies involving multiple sintering aids over a wide sintering-temperature range remain limited. This gap hinders the optimization of processing parameters for high-performance piezoelectric ceramics with complex architectures because different sintering aids may act through different pathways, and their interactions with sintering temperature may strongly influence the resulting microstructure and macroscopic properties. Recent advances in architectured and textured piezoelectric ceramics have further demonstrated that material orientation and structural configuration are important for improving electromechanical performance and device-level functionality [39–41]. Textured honeycomb $BaTiO_3$-based ceramics fabricated by vat photopolymerization have exhibited enhanced piezoelectric and sensing performance, while three-dimensional anti-tetrachiral negative-Poisson's-ratio $BaTiO_3$ structures have shown substantially improved hydrostatic piezoelectric responses [40,41]. However, emphasis in these recent studies has mainly been placed on composition modification, crystallographic texturing, or structural design.

Against this background, DLP was employed as the shaping technique, and tetraethyl orthosilicate (TEOS), silica (SiO_2), lithium carbonate (Li_2CO_3), and copper oxide (CuO) were introduced into a $BaTiO_3$ photosensitive slurry with a solid loading of 85 wt%. The effects of these four sintering aids on the microstructure, phase composition, densification behavior, shrinkage characteristics, and mechanical properties of the ceramics were systematically investigated at five sintering temperatures ranging from 1375 to 1475 °C. Their piezoelectric, dielectric, and ferroelectric responses were also comprehensively evaluated. In addition, finite element analysis was performed to examine the voltage response under ultrasonic-frequency excitation. To address this gap, four representative sintering aids were systematically compared under identical DLP processing conditions over a wide sintering-temperature range. The structure–property relationships among sintering-aid type, sintering temperature, microstructure, and macroscopic performance were investigated to provide an experimental basis for processing optimization and property regulation in additively manufactured $BaTiO_3$ piezoelectric ceramics.

2. Materials and methods

2.1. Raw materials

The photocurable piezoelectric ceramic slurry consisted of three components: $BaTiO_3$ ceramic powder, a photosensitive resin premix, and sintering aids. Commercial barium titanate ($BaTiO_3$) powder (Macklin) was used as the piezoelectric ceramic matrix. Based on a bimodal particle size design, fine powder with an average particle size of 124.4 nm and coarse powder with an average particle size of 669.8 nm were mixed at a predetermined ratio. Both powders exhibited quasi-spherical morphology, normal particle size distributions, and a density of 6.08 g/cm^3 at 25 °C. The bimodal particle system was designed to improve slurry rheology and packing density.

The photosensitive resin premix consisted of a photopolymerizable resin (Shenzhen Adventure Technology Co., Ltd., China), XBPO photoinitiator (Macklin), BYK-111 dispersant (BYK, Germany), and MEHQ inhibitor (Macklin). XBPO initiated polymerization under UV irradiation, BYK-111 improved particle dispersion and reduced sedimentation, and MEHQ suppressed dark polymerization to ensure printing stability.

Copper oxide (CuO), silica (SiO_2), tetraethyl orthosilicate (TEOS), and lithium carbonate (Li_2CO_3) (all purchased from Aladdin) were individually used as sintering aids. Each additive was introduced into the premix at the same mass fraction and then mixed with the $BaTiO_3$ powder to regulate densification behavior and electrical properties.

Fig. 1 shows the morphologies and particle size distributions of the

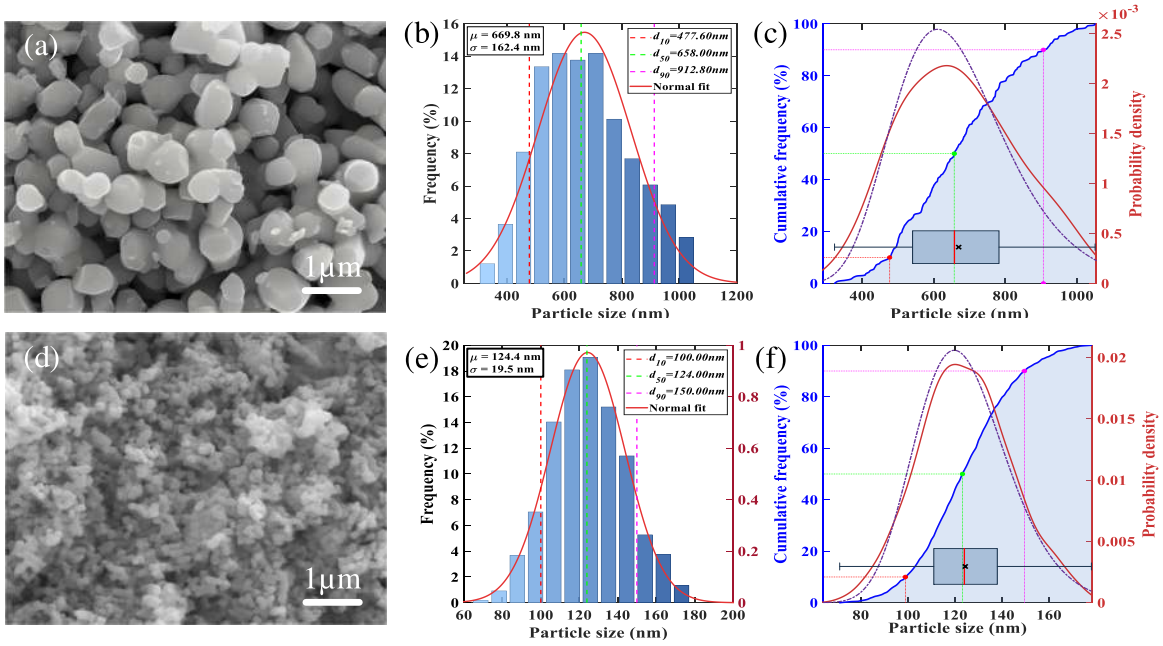

Fig. 1. Characterization of the raw $BaTiO_3$ powders: (a–c) coarse powder, including: (a) SEM morphology. (b) particle size distribution. (c) cumulative distribution curve with box plot. (d–f) fine powder, including: (d) SEM morphology. (e) particle size distribution. (f) cumulative distribution curve with box plot.

two $BaTiO_3$ powders. As shown in Fig. 1(a) and (d), both powders exhibited quasi-spherical morphology, but with distinct particle size characteristics. The coarse powder (BT-Coarse) had an average particle size of 669.4 ± 162.4 nm and a relatively broad distribution, whereas the fine powder (BT-Fine) showed an average particle size of 124.4 ± 19.5 nm and a narrower distribution.

Particle size analysis further confirmed these differences (Fig. 1(c) and (f)). For BT-Coarse, the characteristic sizes were d_{10} = 477.6 nm, d_{50} = 658.0 nm, and d_{90} = 912.8 nm. For BT-Fine, the corresponding values were d_{10} = 100.0 nm, d_{50} = 124.0 nm, and d_{90} = 150.0 nm, indicating a much narrower size range. Box plot analysis also showed that BT-Fine had lower size dispersion (IQR = 27 nm, span = 0.403) than BT-Coarse (IQR = 241.5 nm, span = 0.661), confirming its better size uniformity.

These results indicate that the bimodal powder system, composed of coarse powder (D_{50} = 658 nm) and fine powder (D_{50} = 124 nm), is favorable for interstitial filling and high packing density in the green bodies, providing a suitable basis for subsequent slurry preparation and sintering densification.

2.2. Slurry preparation

The $BaTiO_3$ piezoelectric ceramic slurry was prepared through four steps, including powder mixing, premix preparation, additive incorporation, and ball milling. According to the bimodal particle size distribution theory, fine $BaTiO_3$ powder (average particle size: 124.4 nm) and coarse $BaTiO_3$ powder (average particle size: 669.8 nm) were mixed at a mass ratio of 4:6. The mixed powders were ground in an agate mortar for 10–20 min with intermittent sieving to ensure homogeneous mixing.

The photosensitive resin premix was prepared by heated magnetic stirring. The photopolymerizable resin (HTL) was homogenized with 2 wt% XBPO photoinitiator, 0.5 wt% MEHQ inhibitor, and BYK-111 dispersant at 30 °C for 60 min.

CuO, SiO_2, TEOS, and Li_2CO_3 were individually employed as sintering aids at 2 wt% of the total slurry mass. In addition, 2 wt% Triton X-100, relative to the ceramic powder mass, was added as a surfactant to improve dispersion.

The powder mixture, resin premix, and additives were then ball-milled with zirconia grinding balls at a ball-to-powder ratio of 3:1. The milling procedure was sequentially conducted at 800 r/min for 2 h, 400 r/min for 2 h, and 200 r/min for 4 h. The resulting slurry was subsequently degassed under vacuum at 10 kPa for 10 min and stored in opaque black bottles for later printing.

2.3. DLP 3D printing process

Barium titanate piezoelectric ceramic green bodies were fabricated using top-down DLP 3D printing. In this printing mode, the ceramic slurry was contained in a resin tank, and the build platform gradually descended into the slurry during fabrication. A UV light source irradiated the slurry surface from above, selectively curing the exposed regions in a layer-by-layer manner to form the green body. Meanwhile, a scraper blade was used to level the slurry surface after each layer, thereby ensuring uniform recoating and stable printing.

The $BaTiO_3$ ceramic green bodies were fabricated by DLP. The CAD models of the test specimens were designed in SolidWorks™ and exported as STL files, which were then imported into the slicing software for model arrangement and slicing. The printing parameters were set as follows: layer thickness, 25 μm; exposure time, 5 s; and light intensity, 58 mW/cm^2.

Before printing, the modified $BaTiO_3$ slurry was poured into the resin tank and uniformly distributed. The printing program was then initiated, and the green bodies were fabricated through sequential layer-by-layer photocuring. After printing, the as-printed green bodies were carefully removed for subsequent post-processing.

2.4. Debinding and sintering processes

Photocured 3D-printed ceramic green bodies usually contain a considerable amount of organic components, and the debinding schedule plays a critical role in the subsequent sintering quality. An excessively rapid debinding process may induce cracking, whereas an overly slow process increases processing time and cost. In addition, insufficient debinding temperature may lead to resin carbonization and contamination of the ceramic matrix. Therefore, a rational debinding schedule based on thermogravimetric analysis is essential.

Thermogravimetry (TG) was performed on the as-printed $BaTiO_3$ ceramic green bodies to evaluate the thermal decomposition behavior of

the organic components, as shown in Fig. 2(a) and (b). The specimens were heated from room temperature to 800 °C at a heating rate of 10 °C/min under a high-purity argon atmosphere.

Based on the TG results, a two-step debinding process under argon and air atmospheres was adopted, as illustrated in Fig. 2(c) and (d). In the first step, the green bodies were heated to 400–500 °C at a rate of 1–2 °C/min under argon to allow pyrolysis of the organic resin in an inert atmosphere. In the second step, the atmosphere was switched to air, and the temperature was further increased to 600–800 °C with intermediate holding to remove residual carbon through oxidation. During the entire debinding process, the heating rate was carefully controlled, and holding steps were introduced within critical temperature ranges to avoid defect formation.

After debinding, the specimens were pressurelessly sintered in air at 1375, 1400, 1425, 1450, and 1475 °C, as shown in Fig. 2(e). The heating rate was 5 °C/min, and the dwell time at the target temperature was 2 h, followed by furnace cooling to room temperature. By comparing the sintering behavior of different additive systems at each temperature, the effects of sintering temperature on densification behavior, microstructure evolution, and electrical properties were systematically investigated.

2.5. Material characterization methods

The phase composition of the sintered $BaTiO_3$ ceramics was characterized by X-ray diffractometry (XRD) using Cu Kα radiation over a 2θ range of 10–80°, with a step size of 0.02° and a scanning rate of 2°/min. The microstructures of the raw powders, printed green bodies, debound bodies, and sintered ceramics were examined by scanning electron microscopy (SEM). Before microscopy, the non-conductive specimens were sputter-coated with gold, and observations were conducted at accelerating voltages of 5–15 kV.

The bulk density of the sintered specimens was determined by the Archimedes' method using deionized water as the immersion medium. Three specimens were evaluated for each condition, and the relative density was calculated using the theoretical density of $BaTiO_3$ (6.08 g/cm^3).

Before electrical characterization, the sintered ceramic discs were polished, ultrasonically cleaned, coated with silver electrodes, and heat-treated at 600 °C for 30 min. Electrical poling was conducted in silicone oil under an electric field of 2 kV/mm at 60 °C for 60 min, followed by aging for 24 h. The piezoelectric coefficient (d_{33}) was determined by quasi-static piezoelectric coefficient measurement at 110 Hz using an oscillating force of 0.25 N. Dielectric properties were characterized by impedance spectroscopy over the frequency range of 100 Hz–1 MHz,

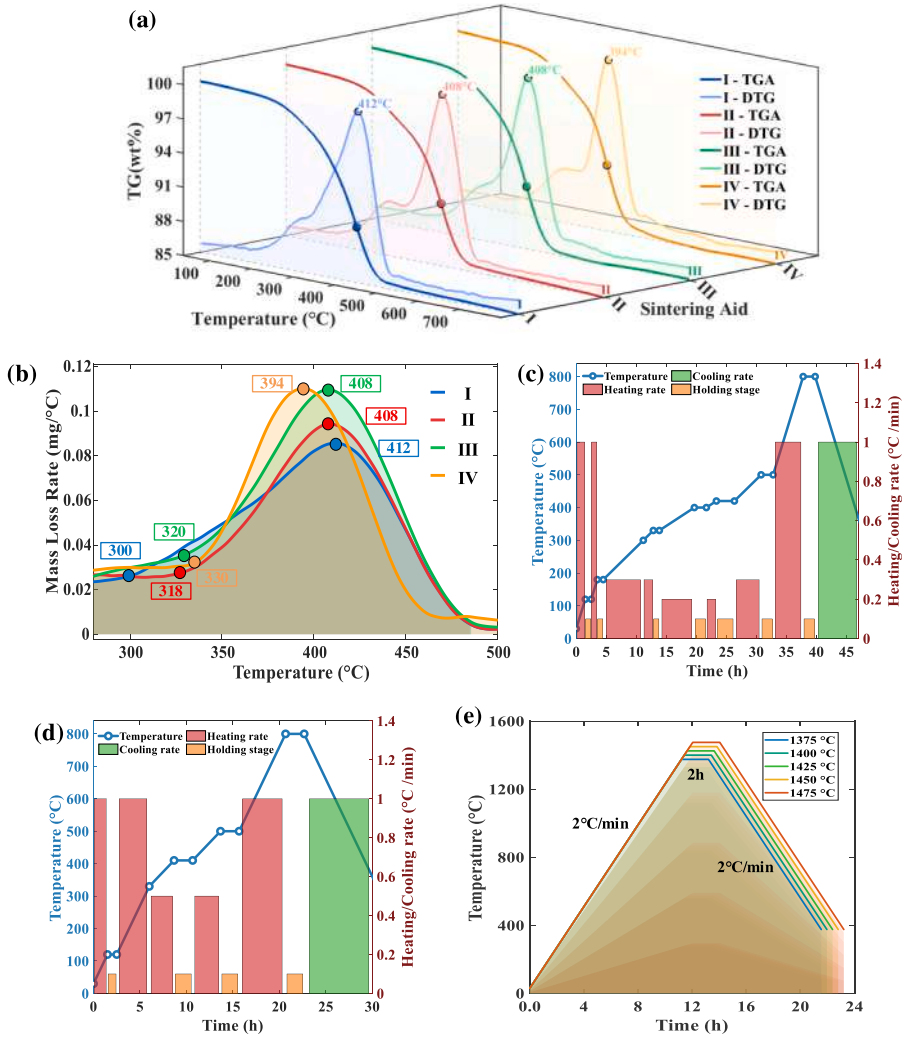

Fig. 2. Thermal behavior of 3D-printed $BaTiO_3$ green bodies with different sintering aids and the corresponding debinding and sintering schedules: (a) TG–DTG curves of green bodies containing four sintering aids (I–IV). (b) DTG curves showing the temperatures of maximum weight-loss rate (T_{max}). (c) temperature profile of the first-step debinding under argon. (d) temperature profile of the second-step debinding in air. (e) sintering schedules at five target temperatures. (For interpretation of the references to colour in this figure legend, the reader is referred to the Web version of this article.)

and the relative permittivity was calculated from the measured capacitance. Ferroelectric hysteresis-loop measurements were performed at 1 Hz to determine the remanent polarization (P_r) and coercive field (E_c).

The surface mechanical properties of the sintered specimens were characterized by instrumented nanoindentation. Before testing, the specimen surfaces were polished to a mirror finish. Nanoindentation measurements were conducted under a maximum load of 500 mN, with a loading and unloading rate of 1000 mN/min and a holding time of 10 s. Three indents were performed on each specimen to determine the hardness, reduced elastic modulus, and corresponding load–displacement responses.

3. Results and discussion

3.1. Phase composition analysis

Fig. 3(a) shows the XRD patterns of $BaTiO_3$ ceramics with four sintering aids sintered at their respective optimum temperatures. All diffraction peaks match well with the standard perovskite $BaTiO_3$ pattern (PDF#05-0626), indicating that the introduction of the sintering aids does not alter the primary phase. The TEOS-, SiO_2-, and CuO-containing specimens exhibit a single perovskite phase without detectable secondary phases. In contrast, a weak Ba_2TiO_4 peak is observed at $2\theta \approx 27.5^\circ$ for the Li_2CO_3-containing specimen, suggesting local compositional segregation caused by Li incorporation.

The piezoelectric response of $BaTiO_3$ is closely related to its tetragonal structure, as evidenced by the splitting of the pseudocubic 200 peak into the tetragonal 002 and 200 peaks at approximately $2\theta = 45^\circ$. As shown in the enlarged patterns, the TEOS- and SiO_2-containing specimens exhibit clear peak splitting, indicating a relatively high tetragonal phase content. By comparison, the Li_2CO_3- and CuO-containing specimens show broader peaks with less distinct splitting, implying weaker tetragonal distortion. This difference is attributed to the distinct effects of dopants on lattice distortion and defect chemistry. Si^{4+} substitution at the Ti site is likely to induce lattice strain and stabilize the tetragonal phase, whereas Li^{+} may introduce oxygen vacancies and Cu^{2+} may lead to more complicated defect states. Accordingly, TEOS and SiO_2 are more effective in retaining the tetragonal structure of $BaTiO_3$, while Li_2CO_3 and CuO tend to reduce tetragonal distortion; among them, the TEOS-containing specimen exhibits the most favorable crystallographic characteristics.

Fig. 3(b) shows the XRD patterns of TEOS-containing $BaTiO_3$ ceramics sintered from 1375 to 1475 °C. All peaks can be indexed to the perovskite $BaTiO_3$ structure, and no secondary phase is detected over the entire temperature range. As the sintering temperature increases from 1375 to 1450 °C, the diffraction intensity gradually increases, indicating improved crystallinity. At 1475 °C, a slight decrease in intensity is observed, which may be related to increased thermal disorder or local volatilization at elevated temperature.

The enlarged view in the inset of Fig. 3(b) further reveals the temperature dependence of the tetragonal distortion. For the specimens sintered at 1375–1425 °C, the diffraction feature at approximately $2\theta = 45^\circ$ remains broad, and the 002/200 doublet is only weakly resolved, indicating relatively weak tetragonal distortion. Clear doublet splitting is observed at 1450 °C, corresponding to the highest tetragonal phase content. When the temperature is further increased to 1475 °C, the peak splitting becomes less pronounced, suggesting a reduction in tetragonal distortion. This behavior is likely associated with the Si-rich liquid phase generated by TEOS decomposition. At 1450 °C, the liquid phase appears to be most beneficial for mass transport and grain growth while maintaining tetragonal stability. At lower temperatures, insufficient liquid-phase mobility may limit densification, whereas at higher temperatures, liquid-phase loss and defect generation may disturb lattice ordering. Therefore, the phase structure of TEOS-containing $BaTiO_3$ is highly sensitive to sintering temperature, with 1450 °C giving the most favorable crystallinity and tetragonal characteristics.

3.2. Sintering densification behavior

3.2.1. Characterization of relative density

Fig. 3(c) shows the relative densities of $BaTiO_3$ ceramics with four sintering aids sintered at 1375–1475 °C. All specimens exhibit an increase–maximum–decrease trend with increasing temperature, although the densification behavior differs markedly with additive type.

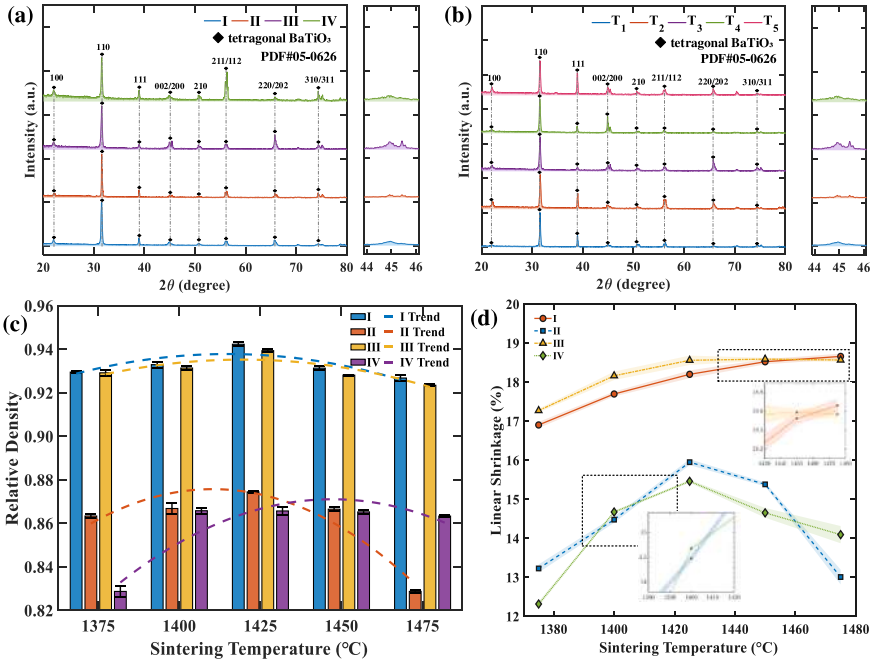

Fig. 3. Phase evolution and densification behavior: (a) XRD patterns of specimens containing different sintering aids at their respective optimal sintering temperatures; (b) phase evolution of the TEOS-containing specimens with increasing sintering temperature; (c) relative density as a function of sintering temperature; and (d) linear shrinkage as a function of sintering temperature.

The CuO- and TEOS-containing specimens reach their maximum relative densities at 1425 °C, with values of 0.9439 and 0.9410, respectively. CuO gives the highest peak density, whereas TEOS shows slightly better stability at higher temperatures. In contrast, the SiO_2-containing specimen exhibits a much lower maximum density of 0.8759 at 1425 °C, with the overall density remaining in the range of 0.83–0.87. The Li_2CO_3-containing specimen reaches its maximum density at 1400 °C (0.8673) and then decreases continuously, showing the weakest densification effect.

The different densification behaviors are associated with the liquid-phase characteristics introduced by the sintering aids. CuO and TEOS likely form liquid phases with suitable viscosity near 1425 °C, which facilitates particle rearrangement and mass transport. At higher temperatures, liquid-phase instability reduces densification efficiency. For SiO_2, insufficient liquid-phase mobility appears to limit densification, whereas Li_2CO_3 may generate a transient Li-rich liquid phase at low temperature but suffer from volatilization and defect formation at higher temperatures. Accordingly, CuO exhibits the most effective densification behavior, closely followed by TEOS, while SiO_2 and Li_2CO_3 show distinctly poorer performance. A sintering temperature of 1425 °C combined with CuO or TEOS is therefore more favorable for obtaining highly densified $BaTiO_3$ ceramics.

3.2.2. Sintering shrinkage behavior

Fig. 3(d) shows the longitudinal shrinkage of $BaTiO_3$ ceramics with four sintering aids sintered at 1375–1475 °C. Shrinkage reflects the effectiveness of particle rearrangement and mass transport during densification.

The TEOS-containing specimens show an increase in shrinkage from 17.27% at 1375 °C to 18.56% at 1425 °C, followed by a stable plateau of 18.5%–18.6% at higher temperatures. The CuO-containing specimens exhibit a continuous increase from 16.91% to 18.66% at 1475 °C, corresponding to the highest shrinkage. By comparison, the SiO_2-containing specimens reach a maximum of 15.95% at 1425 °C and then decrease to 13.01% at 1475 °C. The Li_2CO_3-containing specimens show a similar trend, increasing to 15.46% at 1425 °C and then dropping sharply to 13.97% at 1475 °C.

The TEOS-containing ceramics show shrinkage behavior consistent with their relative density evolution, indicating stable and effective liquid-phase-assisted sintering. In contrast, the CuO-containing ceramics exhibit high shrinkage but do not achieve correspondingly superior densification, suggesting accelerated grain-boundary migration and pore entrapment during sintering. The SiO_2-containing ceramics display a similar trend to the TEOS-containing specimens, but with lower shrinkage values. For Li_2CO_3, the decline in shrinkage at high

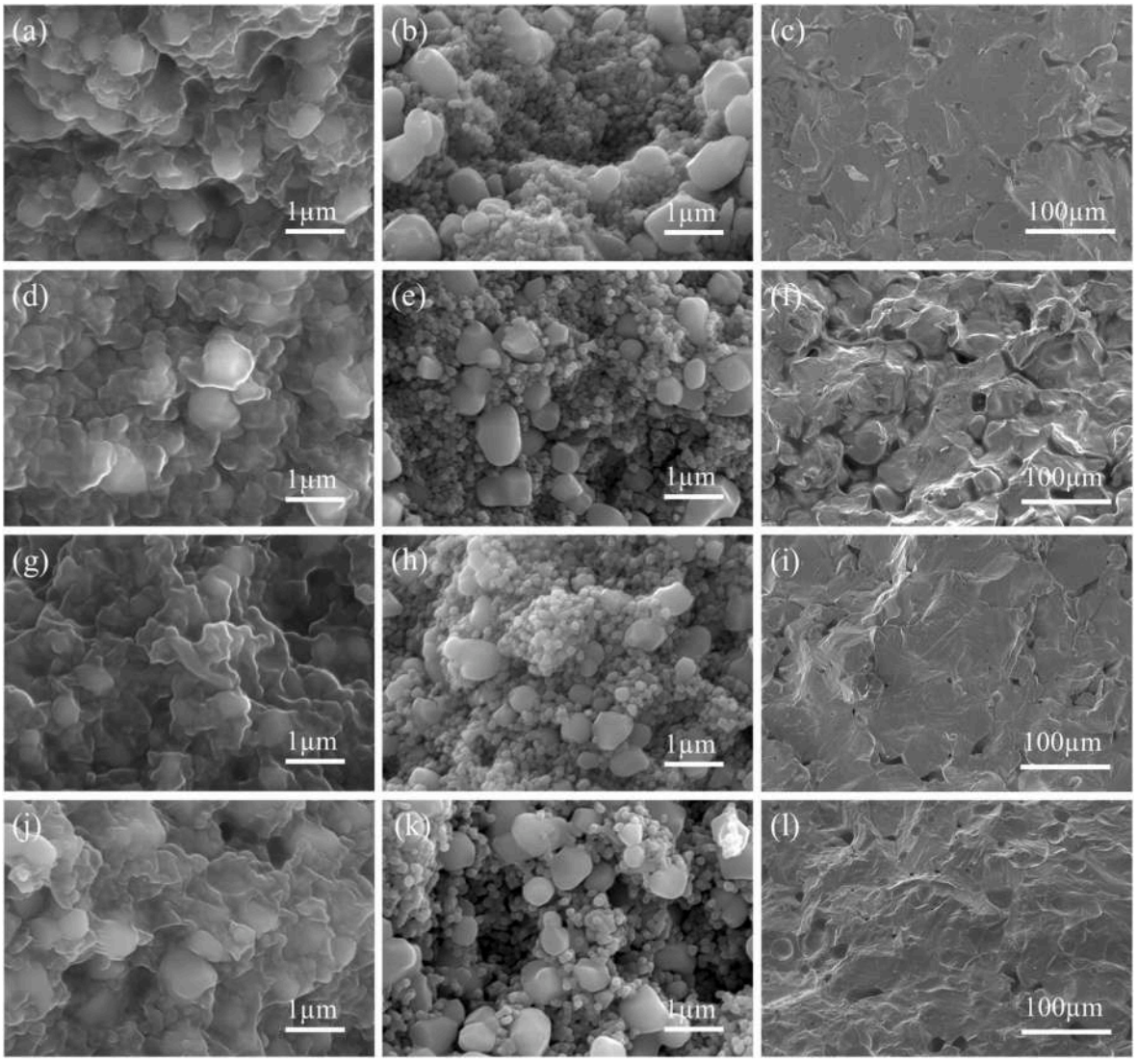

Fig. 4. SEM images of specimens with four sintering aids before debinding, after debinding, and after sintering. Each row corresponds to one additive, from left to right: green body, debound body, and ceramic sintered at 1425 °C: (a–c) Additive I, (d–f) Additive II, (g–i) Additive III, (j–l) Additive IV.

temperature is likely caused by severe volatilization of the liquid phase. Accordingly, TEOS provides the most favorable shrinkage stability above 1425 °C, which is conducive to the formation of a uniform and dense microstructure.

3.3. Characterization of microstructure

3.3.1. Microstructural evolution analysis

Fig. 4 shows the microstructural evolution of $BaTiO_3$ ceramics with four sintering aids at the green, debound, and sintered stages. The sintering aids significantly influence particle packing, grain bonding, and densification behavior.

At the green stage (Fig. 4(a)–(d), (g) and (j)), all specimens exhibit resin-coated lamellar stacking structures. The CuO-containing specimen shows relatively compact particle packing with slight agglomeration, whereas the SiO_2-containing specimen exhibits clear particle boundaries and looser bonding. The TEOS- and Li_2CO_3-containing specimens display folded lamellar morphologies, reflecting the influence of additives on slurry rheology.

After debinding (Fig. 4(b)–(e), (h) and (k)), direct particle contact is established and micropores are formed. The CuO-containing specimen shows fine particles filling the gaps between coarse particles, which is beneficial for subsequent sintering. The SiO_2-containing specimen exhibits agglomeration and large interparticle voids. The TEOS-containing specimen shows a marked increase in fine particles after debinding. This observation is consistent with the possible formation of finely dispersed silica-containing species from TEOS, as reported previously. Such species may contribute to improved particle packing and enhanced densification. However, direct evidence for the formation and distribution of such phases was not obtained, and further characterization is required. The Li_2CO_3-containing specimen presents a relatively uniform particle distribution with evident fine-particle filling.

After sintering at 1425 °C (Fig. 4(c)–(f), (i) and (l)), all specimens undergo grain growth and densification, but their microstructures remain distinct. The CuO-containing specimen forms continuous sintering necks and a relatively dense structure. The SiO_2-containing specimen retains more pores and weaker grain bonding. The TEOS-containing specimen exhibits uniform grains and a dense microstructure with low porosity, whereas the Li_2CO_3-containing specimen shows blurred grain boundaries and reduced porosity. These results indicate that CuO and Li_2CO_3 mainly enhance liquid-phase-assisted diffusion, while the superior densification behavior of the TEOS-containing specimen may be associated with the decomposition products of TEOS and the resulting improvement in particle packing homogeneity. Nevertheless, the underlying mechanism remains a hypothesis and should be further verified through advanced microstructural characterization. In contrast, SiO_2 may hinder full grain contact because of glassy-phase formation. As a result, the TEOS-containing specimen exhibits the most favorable microstructure for polarization and reduced domain-wall pinning.

3.3.2. Microstructural evolution of TEOS-containing $BaTiO_3$ ceramics during sintering

Fig. 5 shows the microstructural evolution of TEOS-containing $BaTiO_3$ ceramics sintered at 1375–1475 °C. With increasing temperature, the grain size gradually increases, the porosity decreases, and the microstructure evolves from a porous state to a dense polycrystalline structure, indicating progressive densification.

At 1375 °C (Fig. 5(a)), the specimen contains numerous irregular pores, together with small and uneven grains, loose intergranular bonding, and poorly developed grain boundaries, indicating an early sintering stage dominated by initial neck formation. At 1400–1425 °C (Fig. 5(b) and (c)), obvious sintering necks develop, the grains become more polyhedral, and large pores progressively shrink or close, resulting in improved structural continuity.

At 1450 °C (Fig. 5(d)), tighter interfacial bonding, clearer grain boundaries, and fewer isolated pores are observed, indicating rapid densification. At 1475 °C (Fig. 5(e)), the microstructure becomes nearly fully dense, with a continuous grain-boundary network and further grain growth.

The observed evolution is associated with the Si-rich liquid phase generated by TEOS decomposition during sintering. This liquid phase promotes grain-boundary diffusion and mass transport, while suppressing abnormal grain growth, thereby improving microstructural uniformity. Overall, the specimens sintered at 1425–1450 °C exhibit the most favorable microstructure, characterized by low porosity, moderate grain size, and clear grain boundaries. This suggests that the liquid phase in this temperature range provides the most suitable balance between densification and grain-growth control, whereas lower temperatures limit liquid-phase activity and higher temperatures may induce grain coarsening. Accordingly, 1425–1450 °C is considered the optimum sintering temperature range for TEOS-containing $BaTiO_3$ ceramics.

3.3.3. Grain size distribution and abnormal grain growth behavior

The apparent grain size distributions were statistically analyzed from SEM images using ImageJ by converting the measured grain areas into

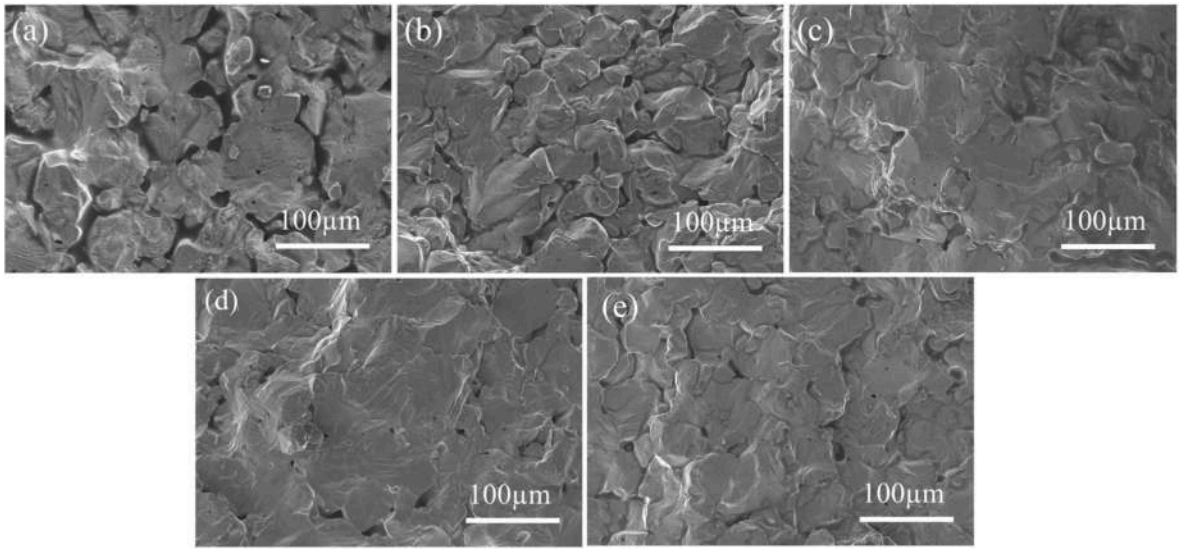

Fig. 5. Effect of sintering temperature on the microstructure of TEOS-containing specimens: (a) 1375 °C, (b) 1400 °C, (c) 1425 °C, (d) 1450 °C, (e) 1475 °C.

equivalent circular diameters. More than 100 grains were evaluated for each sintering condition to ensure statistical reliability. As shown in Fig. 6(d–f) both the average apparent grain size and the distribution width increase with sintering temperature, indicating progressive grain coarsening and enhanced microstructural heterogeneity.

The mean apparent grain size increases from 50.31 μm at 1375 °C to 56.61 μm at 1425 °C, and further to 74.30 μm at 1475 °C, accompanied by an increase in standard deviation. This result suggests that grain growth becomes increasingly nonuniform at elevated sintering temperatures. In particular, the broadened grain size distribution at 1475 °C indicates the occurrence of heterogeneous or abnormal grain growth.

The enhanced grain coarsening in the CuO-containing specimens may be associated with CuO-assisted sintering, which can promote mass transport and increase grain boundary mobility during high-temperature sintering. The possible formation of a transient liquid phase or Cu-related species at grain boundaries may further facilitate localized grain growth, leading to a broader grain size distribution. Similar grain growth behavior has been observed in doped ferroelectric ceramics during sintering, where sintering additives can significantly affect grain boundary mobility and microstructural evolution [11,27,29].

Overall, the grain size statistics indicate that CuO addition can promote densification and piezoelectric response, but excessive grain coarsening at elevated temperatures reduces microstructural uniformity. Such microstructural heterogeneity may influence the stability of functional properties, although direct reliability tests are still required for further verification.

3.4. Characterization of piezoelectric and dielectric properties

3.4.1. Dielectric and resonance response characteristics

Fig. 7(a) shows the amplitude–frequency–phase responses of $BaTiO_3$ ceramics with four sintering aids. All specimens exhibit clear resonance behavior, indicating effective electromechanical coupling after printing and sintering. The resonance frequencies are 279.8 kHz for specimen II, 302.9 kHz for specimen I, 349.4 kHz for specimen IV, and 354.8 kHz for specimen III. These differences indicate that the sintering aids significantly affect the dynamic electrical response of the ceramics.

The admittance-circle curves in Fig. 7(b) show obvious differences in loop size and shape. Specimens III and IV exhibit much larger loops than specimens I and II, indicating stronger resonance activity and greater energy exchange during excitation. In contrast, specimen II shows the smallest loop, suggesting a weaker dielectric response. The phase–frequency curves in Fig. 7(c) further confirm this trend. All specimens show sharp phase reversal near resonance, but specimens III and IV exhibit stronger and broader phase-transition behavior, whereas specimen II shows a narrower and weaker transition region. The amplitude–frequency curves in Fig. 7(d) are consistent with these results, with specimens III and IV showing deeper resonance minima and thus stronger resonance intensity.

These differences are closely related to microstructural uniformity and defect state. A dense and homogeneous microstructure favors continuous polarization pathways and easier domain-wall motion, whereas residual porosity and defect clusters increase internal loss and weaken the resonance response. Therefore, the specimen showing the highest resonance frequency and strongest resonance behavior is considered to have the most favorable microstructural and electrical state. If this specimen corresponds to the TEOS-modified composition, the result is consistent with the previous phase and microstructural analyses. TEOS-assisted sintering appears to simultaneously improve densification, stabilize the tetragonal phase, and reduce domain-wall pinning, thereby leading to superior dielectric and electromechanical response. Accordingly, the resonance results confirm that the sintering aid plays a key role in determining the dielectric response of 3D-printed $BaTiO_3$ ceramics, and the optimum system exhibits a higher resonance frequency, stronger phase reversal, and more efficient electromechanical conversion.

3.4.2. Piezoelectric coefficient

Fig. 7(e) shows the variation in d_{33} of $BaTiO_3$ ceramics with four sintering aids over 1375–1475 °C. All specimens exhibit an increase-then-decrease trend with increasing sintering temperature, indicating that the piezoelectric response is highly sensitive to sintering-induced changes in densification and grain development.

The CuO-containing specimens (I) show the highest peak d_{33}, increasing from 161.7 pC/N at 1375 °C to 258.7 pC/N at 1450 °C,

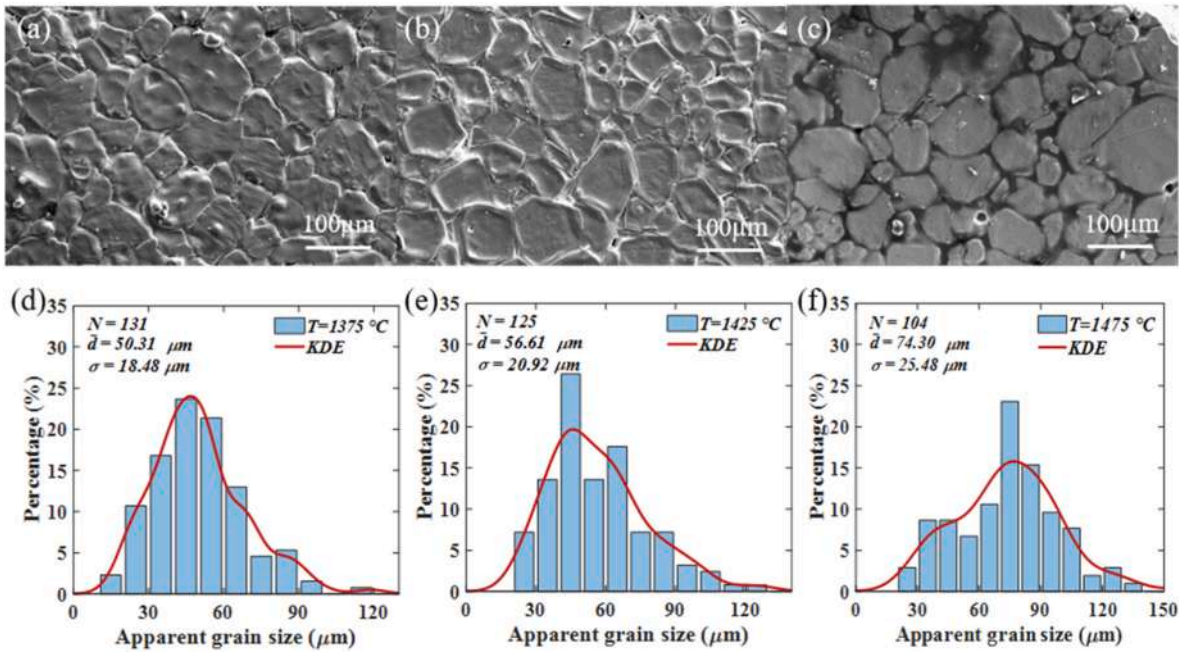

Fig. 6. Temperature-dependent microstructure evolution and grain size statistics of 3D-printed piezoelectric ceramics: (a–c) SEM micrographs showing grain coarsening at increasing sintering temperatures. (d–f) Grain size distributions extracted from SEM images, fitted using kernel density estimation (KDE).

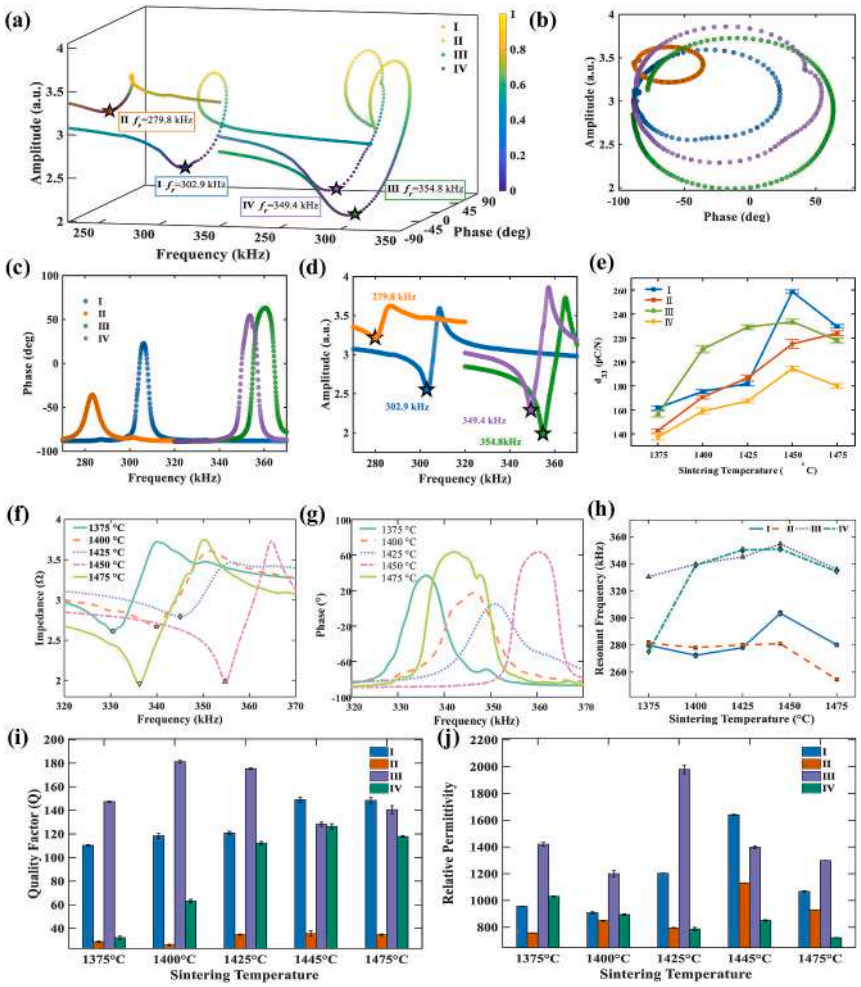

Fig. 7. Dielectric and piezoelectric performance analysis: (a) 3D impedance spectra of four specimens. (b) Admittance circle plot. (c) Amplitude–frequency response. (d) Phase–frequency response. (e) Evolution of piezoelectric coefficient with temperature. (f) Amplitude–frequency curves of TEOS at different temperatures. (g) Phase–frequency curves of TEOS at different temperatures. (h) Temperature dependence of resonant frequency. (i) Temperature dependence of quality factor. (j) Temperature dependence of dielectric constant.

followed by a decrease to 229.7 pC/N at 1475 °C. However, this high d_{33} is accompanied by abnormal grain growth, indicating that the enhanced response is obtained at the expense of microstructural uniformity.

The TEOS-containing specimens (III) exhibit a more balanced behavior, with d_{33} increasing from 156.3 pC/N to 229.0 pC/N at 1425 °C, reaching 233.7 pC/N at 1450 °C, and then decreasing to 218.0 pC/N at 1475 °C. Notably, d_{33} remains above 220 pC/N within 1425–1450 °C, demonstrating a relatively wide processing window. This result is consistent with the dense and uniform microstructure of the TEOS-containing ceramics, which favors polarization alignment and reduces domain-wall pinning. Therefore, despite a slightly lower peak value than CuO, TEOS provides the most favorable overall piezoelectric performance.

The SiO_2-containing specimens (II) show a gradual increase in d_{33} from 142.7 pC/N to 224.0 pC/N at 1475 °C, but their values remain lower than those of the TEOS-containing specimens, likely because of lower density and smaller grain size. The Li_2CO_3-containing specimens (IV) exhibit the lowest d_{33} values throughout the entire temperature range, increasing from 137.3 pC/N to 194.3 pC/N at 1450 °C and then decreasing, which is attributed to residual porosity and the presence of the Ba_2TiO_4 secondary phase. Accordingly, the TEOS-containing ceramics exhibit the best structure–property balance within 1425–1450 °C, identifying TEOS as the most effective sintering aid for improving the piezoelectric performance of the present 3D-printed $BaTiO_3$ ceramics.

3.4.3. *Resonant frequency analysis*

Fig. 7(h) shows the variation in resonant frequency (f_r) of $BaTiO_3$ ceramics with four sintering aids over 1375–1475 °C. As a key electromechanical parameter, f_r is closely related to the elastic response, densification state, and structural integrity of the ceramics.

The TEOS-containing specimens (III) exhibit the highest overall f_r values, increasing from 330.5 kHz at 1375 °C to 354.8 kHz at 1450 °C, followed by a decrease to 336.2 kHz at 1475 °C. Notably, f_r remains in the range of 345–355 kHz within 1425–1450 °C, consistent with the optimum density and microstructural uniformity, indicating a strong elastic response associated with dense and homogeneous grain development.

The Li_2CO_3-containing specimens (IV) show a sharp increase in f_r from 275.3 kHz at 1375 °C to 339.1 kHz at 1400 °C, followed by a high-frequency plateau of 350–351 kHz over 1425–1450 °C, and then a decrease to 334.4 kHz at 1475 °C. This behavior suggests that transient liquid-phase-assisted densification is effective at intermediate temperatures but becomes unstable at higher temperature because of volatilization-induced structural degradation.

The CuO-containing specimens (I) maintain relatively low f_r values of 272–280 kHz from 1375 to 1425 °C, then increase to 303.6 kHz at 1450 °C before decreasing again to 280.2 kHz at 1475 °C. Although the peak temperature matches that of the maximum d_{33}, the overall frequency level remains much lower than those of the TEOS- and Li_2CO_3-containing specimens, suggesting that the microstructural heterogeneity

induced by abnormal grain growth may contribute to the observed frequency variation.

The SiO_2-containing specimens (II) show a nearly constant f_r of 278–282 kHz over 1375–1450 °C, followed by a sharp drop to 254.6 kHz at 1475 °C, indicating insufficient high-temperature stability. Accordingly, the TEOS-containing ceramics exhibit the highest and most stable resonant frequency within 1425–1450 °C, providing further evidence that TEOS is the most effective sintering aid for achieving a dense, uniform, and mechanically stable $BaTiO_3$ ceramic system.

3.4.4. Mechanical quality factor analysis

Fig. 7(i) shows the variation in the mechanical quality factor (Q_m) of $BaTiO_3$ ceramics containing four sintering aids over the sintering temperature range of 1375–1475 °C. Q_m reflects the energy dissipation during resonance and is closely related to domain-wall motion, grain-boundary characteristics, and defect concentration. Its magnitude is also important for device applications, since higher Q_m is generally preferred for high-power devices to reduce heat generation, whereas moderate Q_m combined with high piezoelectric activity is more favorable for receiving-type devices.

The TEOS-containing specimens (III) exhibit the highest Q_m value of 181.2 at 1400 °C, followed by a gradual decrease to 140.6 at 1475 °C. This trend is consistent with the microstructural evolution of the TEOS-containing ceramics, in which uniform grain growth and cleaner grain boundaries facilitate domain-wall motion while simultaneously increasing mechanical loss. Considering that the TEOS system also maintains high d_{33} values in the range of 229–234 pC/N, it shows a favorable balance between piezoelectric activity and mechanical loss, making it more suitable for high-sensitivity receiving-type applications.

The CuO-containing specimens (I) show a continuous increase in Q_m from 110.4 to 152.3 at 1475 °C. The relatively high Q_m is likely associated with defect-induced domain-wall pinning, particularly that related to acceptor-type behavior and oxygen vacancies, which suppresses domain-wall mobility and reduces mechanical loss. Combined with its high d_{33} peak value, the CuO-containing system is therefore more suitable for high-power applications.

The Li_2CO_3-containing specimens (IV) show an increase in Q_m from 32.1 to 126.3 at 1450 °C, indicating reduced defect concentration and improved structural continuity during densification. However, their relatively low d_{33} limits the overall functional performance. By contrast, the SiO_2-containing specimens (II) maintain consistently low Q_m values in the range of 26–36, much lower than those of the other systems, which may be related to increased mechanical loss caused by the formation of a glassy phase. Accordingly, TEOS provides the most favorable combination of Q_m and d_{33} for receiving-type applications, whereas CuO is more advantageous for high-power operation, while Li_2CO_3 and SiO_2 show relatively limited application potential because of their less balanced performance.

3.4.5. Dielectric properties analysis

Fig. 7(j) shows the variation in the relative dielectric constant (ε_r) of $BaTiO_3$ ceramics containing four sintering aids over the sintering temperature range of 1375–1475 °C. As an important dielectric parameter, ε_r reflects the charge-storage capability of the ceramics and is closely related to densification, grain size, and defect concentration.

The TEOS-containing specimens (III) exhibit the highest ε_r value of 1904 at 1425 °C, representing an increase of 34.0% compared with that at 1375 °C, followed by a decrease to 1299 at 1475 °C. The peak temperature coincides well with the optimum density and microstructural state. The dense microstructure suppresses leakage paths, while the uniform fine grains promote polarization response, together resulting in the highest dielectric constant. Therefore, the TEOS-containing ceramics exhibit the most favorable dielectric performance, indicating strong potential for applications requiring high dielectric response.

The CuO-containing specimens (I) show an increase in ε_r from 956 to a maximum of 1640 at 1450 °C, followed by a sharp decrease to 1067 at higher temperature. This decline is consistent with the microstructural changes associated with abnormal grain growth, which can introduce grain-boundary defects and leakage pathways, thereby weakening the dielectric response.

The SiO_2-containing specimens (II) reach a maximum ε_r of 1131 at 1450 °C, but the overall values remain markedly lower than those of the TEOS- and CuO-containing specimens. This behavior is consistent with their lower density and finer grain size, since excessive grain boundaries tend to increase domain-wall pinning and reduce polarization response. The Li_2CO_3-containing specimens (IV) exhibit the lowest overall ε_r values, decreasing from 1030 to 721 at 1475 °C. This poor dielectric performance is associated with the porous microstructure and the presence of the Ba_2TiO_4 secondary phase, both of which are unfavorable for stable dielectric polarization. Accordingly, among the four systems, TEOS provides the most effective enhancement in dielectric properties, with the optimum performance achieved at 1425 °C.

3.5. Characterization of ferroelectric properties

3.5.1. Determination of testing electric field

To determine an appropriate electric field for ferroelectric characterization, representative specimens were first measured under different applied electric fields, as shown in Fig. 8(a–c). With increasing electric field from 10 to 35 kV/cm, the hysteresis loops gradually approached saturation, while both the remanent polarization (P_r) and coercive field (E_c) increased continuously.

As shown in Fig. 8(a), the hysteresis loops measured below 20 kV/cm are relatively narrow, indicating incomplete polarization switching. When the electric field reaches 25 kV/cm, the loops become nearly saturated. Further increasing the field leads only to limited improvement in P_r and E_c, as shown in Fig. 8(b), while the experimental fluctuation becomes more pronounced. At the same time, the loop asymmetry remains relatively low at 25 kV/cm (Fig. 8(c)), indicating good measurement stability and reliability. Therefore, 25 kV/cm was selected as the standard testing electric field for subsequent ferroelectric measurements, as it provides a suitable balance between polarization saturation, measurement accuracy, and electrical safety.

3.5.2. Effect of sintering aids on ferroelectric hysteresis behavior

Fig. 9(a–d) shows the ferroelectric hysteresis loops (P–E loops) of $BaTiO_3$ ceramics containing four sintering aids, measured at 25 kV/cm. The marked differences in loop shape and polarization intensity indicate that the sintering aids strongly affect ferroelectric switching through their regulation of microstructure.

The CuO-containing system (I) exhibits the broadest loops and relatively high saturation polarization, particularly at 1425 °C. This behavior is associated with enhanced domain-wall mobility induced by grain growth, although the relatively full loop shape also suggests a contribution from leakage conduction.

The TEOS-containing system (III) exhibits high polarization intensity, good loop squareness, and comparatively stable hysteresis behavior over the investigated temperature range, with the maximum polarization observed at 1450 °C. This result is consistent with its dense and uniform microstructure, which reduces local electric-field inhomogeneity and facilitates more complete domain switching. The Li_2CO_3-containing system (IV) shows relatively high polarization, but the loops at different temperatures overlap more strongly, indicating weaker temperature dependence. In contrast, the SiO_2-containing system (II) exhibits narrow loops with the lowest polarization intensity, which is directly related to its porous microstructure and the corresponding suppression of effective electric-field distribution and domain-wall motion. All four systems show their highest polarization response near 1450 °C, consistent with the temperature dependence of d_{33}, confirming that appropriate grain development and densification dominate the ferroelectric response. Among them, the TEOS-containing ceramics show the best balance between polarization intensity, loop squareness,

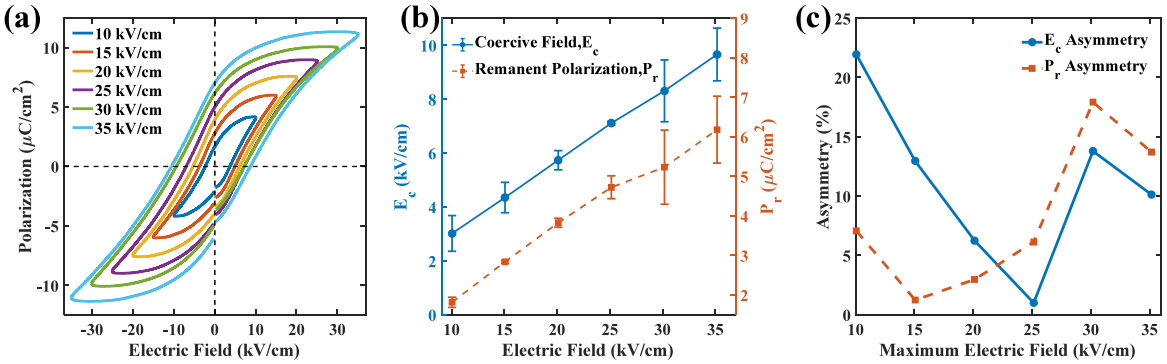

Fig. 8. Determination of the testing electric field for ferroelectric characterization of $BaTiO_3$ ceramics: (a) polarization–electric field (P–E) hysteresis loops measured under different electric fields. (b) coercive field (E_c) and remanent polarization (P_r) as functions of electric field. (c) loop asymmetry as a function of electric field.

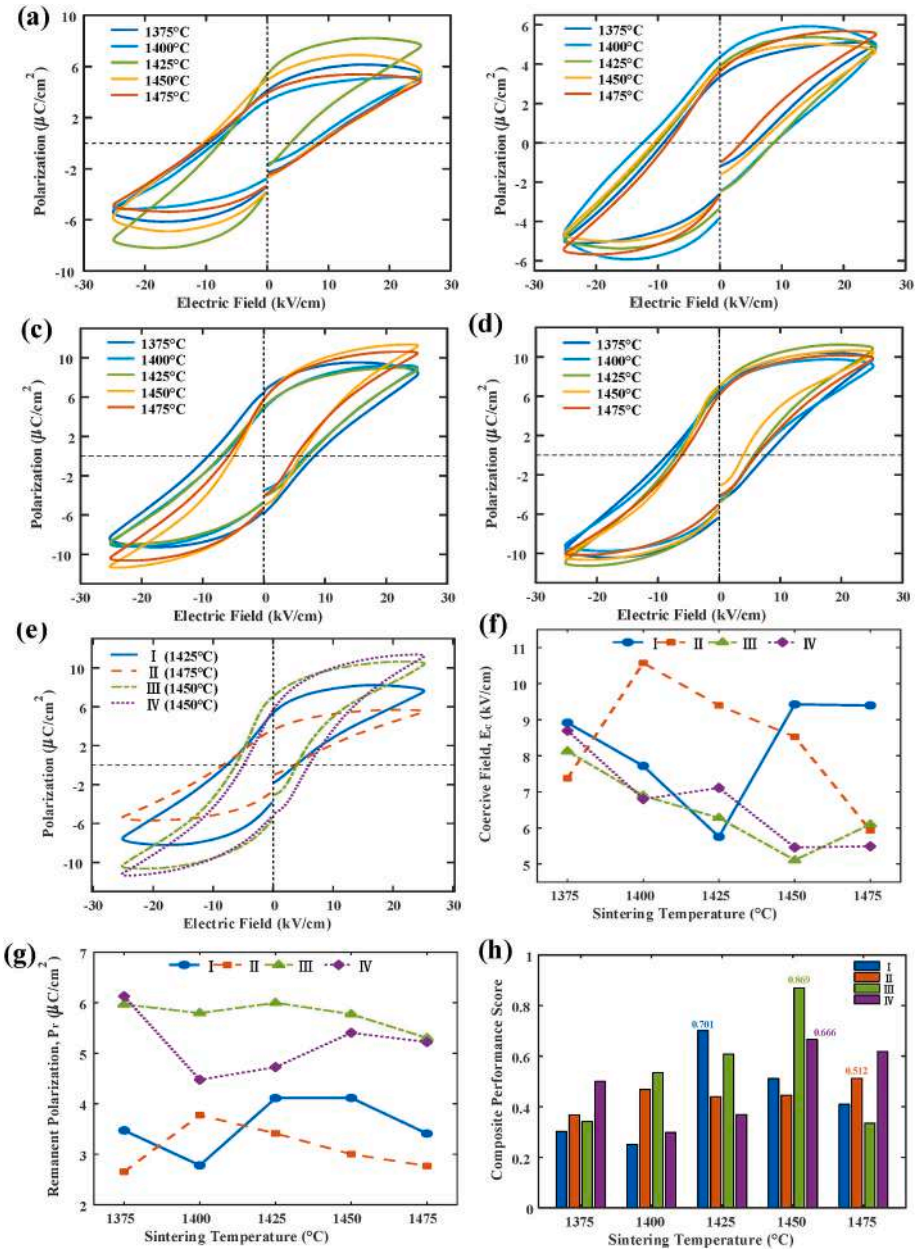

Fig. 9. Comparison of ferroelectric responses of $BaTiO_3$ ceramics containing different sintering aids: (a–d) P–E hysteresis loops of the four sintering-aid systems measured at 25 kV/cm (e) comparison of P–E hysteresis loops of the four systems at their respective optimum sintering temperatures. (f) coercive field (E_c) as a function of sintering temperature. (g) remanent polarization (P_r) as a function of sintering temperature. (h) comprehensive performance score of the four systems.

and temperature stability, indicating the strongest structure–property correlation.

3.5.3. Comparative ferroelectric performance of different sintering aid systems at optimal temperatures

Fig. 9(e) shows the ferroelectric hysteresis loops of $BaTiO_3$ ceramics containing four sintering aids at their respective optimum sintering temperatures, namely TEOS (1450 °C), Li_2CO_3 (1450 °C), CuO (1425 °C), and SiO_2 (1475 °C). The marked differences in loop shape and polarization intensity clearly demonstrate the distinct effects of the sintering aids on the ferroelectric response.

In terms of polarization intensity, the TEOS- and Li_2CO_3-containing systems exhibit the highest saturation polarization among the four compositions. The TEOS-containing specimen shows the most complete loop with the best squareness, indicating more efficient domain switching and lower switching resistance. Although the Li_2CO_3-containing specimen exhibits slightly higher saturation polarization, its loop slope and symmetry are inferior to those of the TEOS-containing specimen, suggesting less stable polarization reversal. The CuO-containing system exhibits an intermediate ferroelectric response, with a relatively high polarization level at 1425 °C, but the rounded loop end indicates that the grain-boundary characteristics associated with liquid-phase sintering may limit the high-field response. In contrast, the SiO_2-containing system shows the weakest ferroelectric performance. Even at 1475 °C, its polarization intensity remains much lower than those of the other systems, and the loop is notably narrow, which is consistent with the suppression of the effective electric field caused by its porous microstructure.

The hysteresis-field characteristics also differ significantly among the four systems. The TEOS-containing specimen exhibits a moderate hysteresis field together with a steep loop profile, indicating that the material can be polarized relatively easily while maintaining a stable ferroelectric state. By comparison, the CuO-containing specimen shows a larger hysteresis field, implying a higher energy barrier for domain switching. Therefore, although the CuO-containing system exhibits the highest peak d_{33} value, the TEOS-containing system provides the most balanced ferroelectric performance in terms of loop quality, polarization stability, and switching efficiency. Combined with its high density and uniform microstructure, TEOS can be regarded as the most effective sintering aid for achieving superior overall ferroelectric performance in the present 3D-printed $BaTiO_3$ ceramics.

3.5.4. Ferroelectric properties analysis

Fig. 9(f) and (g) show the variation in coercive field (E_c and remanent polarization (P_r)) of $BaTiO_3$ ceramics containing four sintering aids over the sintering temperature range of 1375–1475 °C. E_c reflects the difficulty of domain switching, whereas P_r represents the retained polarization after removal of the electric field. Together, these two parameters determine the ferroelectric performance of the ceramics.

The TEOS-containing specimens (III) exhibit consistently low E_c values, decreasing from 8.13 kV/cm at 1375 °C to a minimum of 5.11 kV/cm at 1450 °C, followed by a slight increase to 6.10 kV/cm at 1475 °C. Notably, E_c remains within 5.1–6.3 kV/cm over 1425–1475 °C, indicating relatively easy domain switching. This behavior is attributed to the dense and uniform microstructure of the TEOS-containing ceramics, in which clean grain boundaries and low defect concentration facilitate domain-wall motion. In contrast, the CuO-containing specimens (I) show a decrease in E_c to 5.76 kV/cm at 1425 °C, followed by a sharp increase to 9.43 kV/cm at 1450 °C and persistently high values at higher temperature, suggesting stronger domain-wall pinning associated with grain-boundary defects induced by abnormal grain growth. The SiO_2-containing specimens (II) exhibit pronounced fluctuations in E_c, reaching a maximum of 10.57 kV/cm at 1400 °C and then decreasing to 5.93 kV/cm at 1475 °C, which is likely related to the large number of grain boundaries associated with their finer grains. The Li_2CO_3-containing specimens (IV) show a gradual decrease in E_c from 8.70 kV/cm to 5.46 kV/cm at 1450 °C, followed by stabilization, which is consistent with transient liquid-phase-assisted densification and subsequent volatilization-induced structural instability.

The TEOS-containing specimens (III) also exhibit the highest P_r values, remaining at 5.8–6.0 μC/cm^2 over 1375–1450 °C and decreasing only slightly to 5.30 μC/cm^2 at 1475 °C. This high P_r is closely associated with the dense and homogeneous microstructure, in which fine equiaxed grains facilitate polarization alignment and clean grain boundaries minimize charge loss. The CuO-containing specimens (I) show peak P_r values of 4.1–4.2 μC/cm^2 at 1425–1450 °C, but the overall level remains lower than that of the TEOS-containing system, indicating that abnormal grain growth does not favor stable remanent polarization. The SiO_2-containing specimens (II) exhibit the lowest P_r values (2.6–3.8 μC/cm^2), which is consistent with their lower density and finer grain structure, both of which are unfavorable for stable domain alignment. The Li_2CO_3-containing specimens (IV) show a decrease in P_r from 6.13 μC/cm^2 at 1375 °C to 4.5–5.4 μC/cm^2 above 1400 °C, suggesting that although the low-temperature liquid phase temporarily enhances polarization, its subsequent volatilization deteriorates ferroelectric stability. Overall, the TEOS-containing ceramics exhibit the most favorable combination of low E_c and high P_r within 1425–1450 °C, indicating easy polarization reversal together with strong charge retention. By comparison, the CuO-containing system shows acceptable ferroelectric performance only near 1425 °C, whereas the SiO_2- and Li_2CO_3-containing systems exhibit relatively weak overall ferroelectric behavior. Therefore, TEOS can be identified as the most effective sintering aid for optimizing the ferroelectric properties of the present 3D-printed $BaTiO_3$ ceramics, with an optimum sintering window of 1425–1450 °C.

3.5.5. Effect of sintering temperature on ferroelectric and dielectric properties of TEOS-containing system

Fig. 10(a–c) shows the evolution of ferroelectric hysteresis behavior and the corresponding electrical parameters, including remanent polarization (P_r), saturation polarization (P_s), coercive field (E_c), and dielectric loss tangent (tanδ), as a function of sintering temperature for TEOS-containing $BaTiO_3$ ceramics.

The temperature-dependent electrical behavior of $BaTiO_3$-based ceramics has been extensively investigated and is closely associated with the ferroelectric–paraelectric phase transition near the Curie temperature (~120 °C), which strongly affects the polarization and dielectric responses [42–44]. Because emphasis was placed on the effects of sintering aids and sintering temperature on the microstructure and room-temperature functional properties of $BaTiO_3$ ceramics fabricated by DLP, direct temperature-dependent electrical measurements under service conditions were not included in the experimental scope. Temperature-dependent electrical behavior and long-term stability should be systematically evaluated in future investigations through direct electrical measurements, thermal-cycling tests, and aging tests. With increasing sintering temperature from 1375 to 1450 °C, both P_r and P_s increase progressively and reach their maximum values at 1450 °C. This indicates that the enhanced densification and grain growth at this temperature promote domain alignment and increase the fraction of switchable ferroelectric domains. When the sintering temperature is further increased to 1475 °C, both polarization parameters decrease slightly, which can be attributed to abnormal grain growth and the associated internal stress concentration, leading to a deterioration of domain stability.

At the same time, Ec decreases markedly with increasing sintering temperature and reaches its minimum value at 1450 °C, indicating reduced resistance to domain switching and enhanced ferroelectric reversibility. This behavior suggests that the TEOS-containing ceramics exhibit the most favorable polarization-switching characteristics at this temperature.

The dielectric loss tangent decreases with increasing sintering temperature and reaches a relatively low value at 1450 °C, indicating reduced dielectric relaxation and energy dissipation in the TEOS-

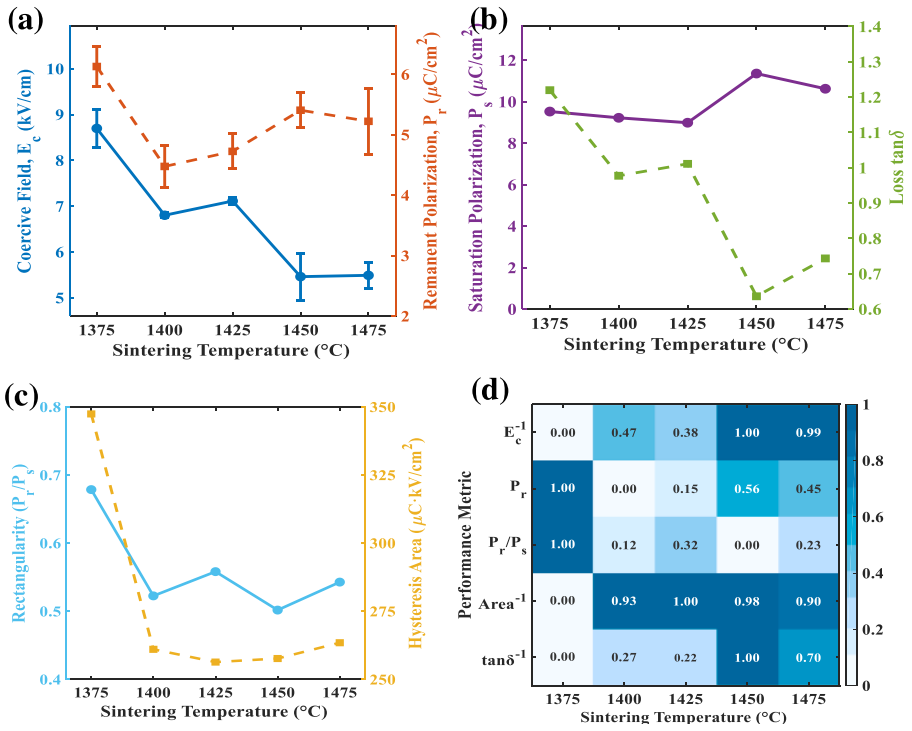

Fig. 10. Sintering-temperature-dependent ferroelectric, dielectric and energy-storage properties of TEOS-containing $BaTiO_3$ ceramics: (a) coercive field (E_c) and remanent polarization (P_r) as functions of sintering temperature. (b) saturation polarization (P_s) and dielectric loss tangent as functions of sintering temperature. (c) loop squareness as a function of sintering temperature. (d) performance heat map.

containing specimens. This behavior is consistent with the formation of a relatively dense and uniform microstructure, which can reduce pore-related interfacial polarization and defect-assisted charge accumulation. When the sintering temperature further increases to 1475 °C, tanδ increases again, which may be associated with localized volatilization, defect generation, or microstructural deterioration under excessive sintering conditions. Therefore, 1450 °C is favorable for achieving low dielectric loss and improved polarization response in the TEOS-containing system. Considering the density, dielectric constant, piezoelectric coefficient, and dielectric loss together, the optimal processing window for the TEOS-containing ceramics is identified as 1425–1450 °C rather than a single optimum temperature.

3.5.6. *Comprehensive performance evaluation and sintering aid selection*

To quantitatively assess the effect of different sintering aids on the overall performance of $BaTiO_3$ ceramics, a multi-parameter composite scoring system was established based on normalized indicators, including the piezoelectric coefficient (d_{33}), remanent polarization (P_r), coercive field (E_c), dielectric loss, and microstructural uniformity. The corresponding results are shown in Fig. 10(d). Compared with evaluation based on a single parameter, this approach provides a more comprehensive assessment of the engineering potential of the ceramics.

The TEOS-containing specimens (III) exhibit the highest composite score of 0.869 at 1450 °C, significantly outperforming the other additive systems. This result indicates that the TEOS system simultaneously maintains high piezoelectric activity (d_{33} = 233.7 pC/N), low coercive field, high remanent polarization, and excellent microstructural stability, thereby achieving the most effective synergy between electrical performance and structural integrity. The CuO-containing specimens (I) reach a maximum score of 0.701 at 1425 °C, confirming the effectiveness of CuO in promoting liquid-phase-assisted densification at relatively low temperature. However, when the sintering temperature exceeds 1450 °C, abnormal grain growth induces structural deterioration, leading to a sharp decrease in score to 0.520 at 1450 °C and 0.410 at 1475 °C, which indicates reduced performance consistency at elevated temperatures. The Li_2CO_3-containing specimens (IV) show relatively stable performance, with a maximum score of 0.666 at 1450 °C. Although the score varies less strongly with temperature, it remains consistently lower than that of the TEOS-containing system, which is consistent with the performance limitations imposed by the loose microstructure and the presence of a secondary phase. By contrast, the SiO_2-containing specimens (II) exhibit the lowest overall scores, with a maximum of only 0.512 at 1475 °C, further confirming that the addition of SiO_2 alone is insufficient to provide effective overall optimization of the $BaTiO_3$ system.

The temperature-dependent variation of the composite performance score further highlights the distinct processing sensitivity of the four systems. In particular, the TEOS-containing ceramics exhibit a pronounced inverted U-shaped trend, reaching a maximum at 1450 °C and decreasing rapidly at higher temperatures. This behavior indicates that the overall performance of the TEOS system is highly sensitive to sintering temperature, and that 1450 °C represents the critical processing condition for fully activating its structure–property synergy.

Therefore, among the four sintering aids investigated, TEOS is identified as the most effective additive for improving the overall performance of the DLP-fabricated $BaTiO_3$ ceramics. Rather than a single optimum temperature, a processing window of 1425–1450 °C is identified, where the ceramics exhibit the most balanced combination of densification, dielectric response, piezoelectric activity, and microstructural stability.

Motivated by recent advances in additively manufactured piezoelectric ceramics [24,37], four representative sintering aids were systematically compared under identical DLP processing conditions over a wide sintering-temperature range. The results demonstrate that the synergistic optimization of additive chemistry and thermal processing is essential for achieving high-performance piezoelectric ceramics with complex geometries. This finding is consistent with recent reports on architectured piezoelectric materials, in which microstructural engineering has been identified as an important link between material design and functional performance.

3.6. Effect of sintering aids on micromechanical behavior

Fig. 11(a–d) shows the nanoindentation results of $BaTiO_3$ ceramics containing four sintering aids, including the load–displacement curves, hardness (H), and elastic modulus (E).

For the TEOS-containing system (Fig. 11(a) and (c)), the indentation depth decreases progressively as the sintering temperature increases from 1375 to 1450 °C, accompanied by a simultaneous increase in hardness and elastic modulus. Both parameters reach their maximum values at 1450 °C, with H ≈ 6.5 GPa and E ≈ 105 GPa. This enhancement is attributed to improved densification and stronger grain-boundary bonding. When the temperature is further increased to 1475 °C, both hardness and elastic modulus decrease markedly, indicating mechanical degradation caused by over-sintering, which may be associated with local microstructural loosening or microcrack formation.

A comparison of the four systems at their respective optimum sintering temperatures is shown in Fig. 11(b) and (d). The TEOS-containing specimen (III) exhibits the highest elastic modulus (approximately 105 GPa) together with relatively stable hardness, indicating the most favorable resistance to local deformation. This behavior suggests that the Si-containing phase introduced by TEOS contributes to a more uniform and mechanically robust microstructure during sintering. Although the SiO_2-containing specimen (II) also exhibits a relatively high elastic modulus, its lower hardness and larger fluctuation indicate inferior mechanical uniformity, which is consistent with the porous microstructure observed by SEM. The CuO-containing specimen (I) shows intermediate mechanical properties, suggesting that abnormal grain growth and the associated internal stress concentration restrict further mechanical improvement. Overall, TEOS modification not only enhances the electrical performance of $BaTiO_3$ ceramics, but also provides a high-modulus and high-hardness microstructural framework, which is beneficial for the mechanical reliability of the device.

3.7. Printing of ultrasonic elements with micron-level precision

Fig. 12 shows the macroscopic morphology of piezoelectric ceramic specimens with two printed architectures at different fabrication stages. Both structures retain good geometric integrity and surface quality in the as-printed state, indicating that DLP is suitable for the fabrication of complex piezoelectric ceramic components. After debinding, only slight darkening is observed, suggesting effective removal of organic species. After sintering, obvious shrinkage occurs, but no visible cracking or deformation is detected, confirming the feasibility of the debinding and sintering process. Compared with structure A, structure B exhibits a denser post-sintering surface, which may be associated with a geometry more favorable for densification.

To clarify the electromechanical response, structure B was further analyzed by finite element simulation using COMSOL Multiphysics. The simulated stress distribution shows that the stress is concentrated near the excitation region, with a maximum value of about 202 Pa, indicating effective acoustic-to-mechanical energy conversion. The simulated voltage response exhibits a peak value of approximately 10 mV, and the electric potential distribution shows clear symmetry between the top and bottom surfaces, consistent with the stress field.

The experimental voltage output measured under ultrasonic excitation reaches about 9.77 mV, which agrees well with the simulated result. Although some harmonic components are present in the measured signal, likely due to local microstructural heterogeneity and nonlinear response, the overall agreement between experiment and simulation confirms both the energy-harvesting capability of the printed $BaTiO_3$ ceramics and the validity of the simulation model.

4. Conclusion

The effects of four sintering aids (TEOS, SiO_2, Li_2CO_3, and CuO) and sintering temperature (1375–1475 °C) on the densification,

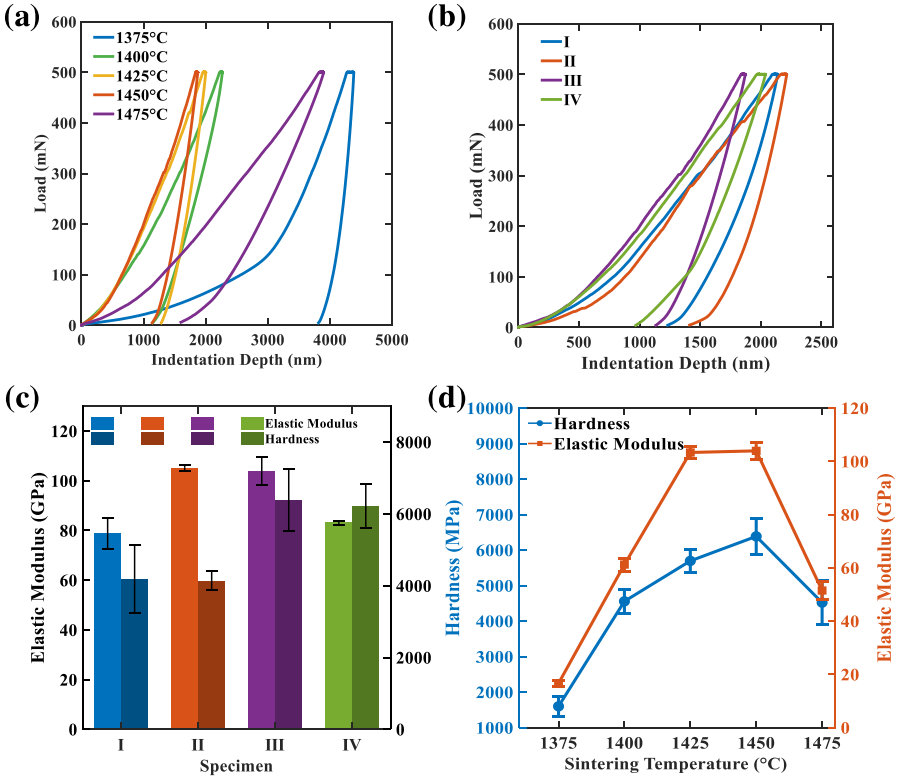

Fig. 11. Nanoindentation mechanical properties characterization: (a) load-unload curves of TEOS system at various temperatures. (b) load-unload curves of four aids at optimal temperatures. (c) hardness and elastic modulus of TEOS as functions of temperature. (d) comparison of hardness and elastic modulus of four aids at optimal temperatures.

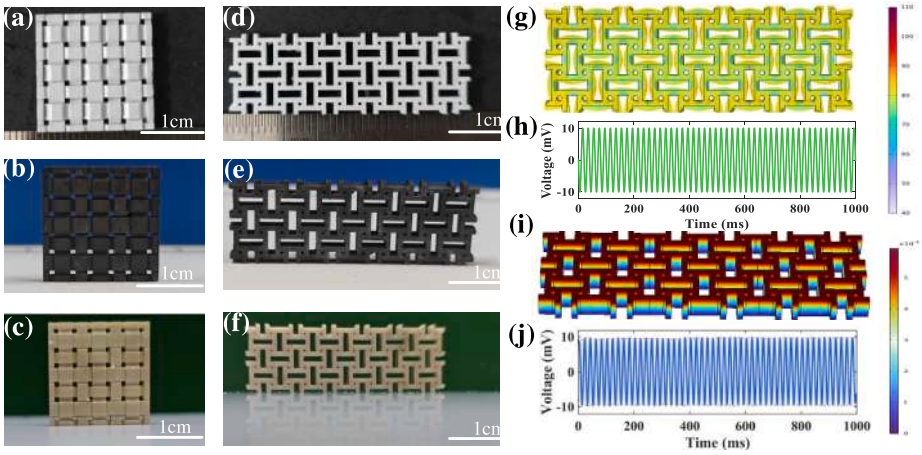

Fig. 12. Preparation process, simulation analysis and energy harvesting performance characterization of 3D printed piezoelectric ceramics. (a–c) printed state, debinding state and sintered state of structure A. (d–f) printed state, debinding state and sintered state of structure B. (g) simulation stress distribution. (h) simulation potential difference curve. (i) simulation potential distribution cloud map. (j) experimental output voltage curve.

microstructure, electrical properties, and mechanical performance of DLP-fabricated $BaTiO_3$ piezoelectric ceramics were investigated. The main conclusions are as follows.

(1) All four sintering aids influenced the densification behavior and microstructural evolution of the printed $BaTiO_3$ ceramics. The resulting electrical, dielectric, ferroelectric, and mechanical properties varied with both the type of sintering aid and the sintering temperature.
(2) The TEOS-containing specimens exhibited the most balanced overall performance. The highest relative density and dielectric constant were obtained at 1425 °C, while the highest piezoelectric coefficient (d_{33}) was achieved at 1450 °C. The optimal processing window for TEOS-containing ceramics was therefore identified as 1425–1450 °C.
(3) The CuO-containing specimens showed the highest peak d_{33} value (258.7 pC/N), indicating the effectiveness of CuO in promoting sintering and piezoelectric response. However, significant grain coarsening was observed at elevated temperatures, resulting in reduced microstructural uniformity.
(4) The Li_2CO_3- and SiO_2-containing specimens exhibited lower overall performance compared with the TEOS-containing system, owing to their less favorable densification and microstructural characteristics.

CRediT authorship contribution statement

Yaxiang Sun: Conceptualization, Data curation, Formal analysis, Investigation, Visualization, Writing – original draft, Writing – review & editing. **Peipei Wang:** Data curation, Writing – review & editing. **Weikai Shi:** Validation, Writing – review & editing. **Xin Lan:** Methodology, Supervision, Writing – review & editing. **Yanju Liu:** Conceptualization, Investigation, Writing – review & editing. **Jinsong Leng:** Investigation, Supervision, Writing – review & editing.

Declaration of competing interest

The authors declare that they have no known competing financial interests or personal relationships that could have appeared to influence the work reported in this paper.

Acknowledgment

This research was supported by National Natural Science Foundation of China (No. 12272113).

References

[1] Z. Jiang, L. Cheng, Y. Zeng, Z. Zhang, Y. Zhao, P. Dong, J. Chen, 3D printing of porous scaffolds $BaTiO_3$ piezoelectric ceramics and regulation of their mechanical and electrical properties, Ceram. Int. 48 (2022) 6477–6487, https://doi.org/10.1016/j.ceramint.2021.11.192.
[2] Z. Wang, X. Yuan, J. Yang, Y. Huan, X. Gao, Z. Li, H. Wang, S. Dong, 3D-printed flexible, Ag-coated PNN-PZT ceramic-polymer grid-composite for electromechanical energy conversion, Nano Energy 73 (2020) 104737, https://doi.org/10.1016/j.nanoen.2020.104737.
[3] L. Taïbi-Benziada, Effect of lithium fluoride on the dielectric properties of barium titanate, Arabian J. Sci. Eng. 39 (2014) 6635–6642, https://doi.org/10.1007/s13369-014-1195-3.
[4] K. Liu, J. Hu, Y. Du, Y. Shi, Y. Sun, S. Zhang, R. Tu, Q. Zhang, S. Huang, H. Sun, Influence of particle size on 3D-printed piezoelectric ceramics via digital light processing with furnace sintering, Int. J. Appl. Ceram. Technol. 19 (2022) 2461–2471, https://doi.org/10.1111/ijac.14074.
[5] S. Guan, H. Yang, Y. Zhao, R. Zhang, Effect of Li_2CO_3 addition in $BiFeO_3$–$BaTiO_3$ ceramics on the sintering temperature, electrical properties and phase transition, J. Alloys Compd. 735 (2018) 386–393, https://doi.org/10.1016/j.jallcom.2017.11.156.
[6] Z. Chen, X. Song, L. Lei, X. Chen, C. Fei, C.T. Chiu, X. Qian, T. Ma, Y. Yang, K. Shung, Y. Chen, Q. Zhou, 3D printing of piezoelectric element for energy focusing and ultrasonic sensing, Nano Energy 27 (2016) 78–86, https://doi.org/10.1016/j.nanoen.2016.06.048.
[7] M.S. Alkathy, A. Hezam, K.S.D. Manoja, J. Wang, C. Cheng, K. Byrappa, K.C. J. Raju, Effect of sintering temperature on structural, electrical, and ferroelectric properties of lanthanum and sodium co-substituted barium titanate ceramics, J. Alloys Compd. 762 (2018) 49–61, https://doi.org/10.1016/j.jallcom.2018.05.138.
[8] M.S. Alkathy, F.L. Zabotto, F.P. Milton, E.R. Botero, M.K. Gatasheh, J.P. Goud, J. A. Eiras, Effect of sintering temperature on structural, electrical, and ferroelectric properties of neodymium and sodium co-doped barium titanate ceramics, J. Mater. Sci. Mater. Electron. 34 (2023) 1144, https://doi.org/10.1007/s10854-023-10576-7.
[9] A. Sood, M. Desseigne, A. Dev, L. Maurizi, A. Kumar, N. Millot, S.S. Han, A comprehensive review on barium titanate nanoparticles as a persuasive piezoelectric material for biomedical applications: prospects and challenges, Small 19 (2023) 2206401, https://doi.org/10.1002/smll.202206401.
[10] B.C. Kim, K.W. Chae, C.I. Cheon, Effect of sintering temperature on the ferroelectric properties and the electro-caloric effect in barium-titanate ceramics, J. Kor. Phys. Soc. 76 (2020) 226–230, https://doi.org/10.3938/jkps.76.226.
[11] W.D. Fei, D. Xu, W.L. Li, L.D. Wang, W. Wang, Electrical properties of AlN and SiO_2 co-modified barium titanate lead-free piezoelectric ceramics, Ferroelectrics 490 (2016) 36–42, https://doi.org/10.1080/00150193.2015.1071130.
[12] P. Kumari, R.K. Gangwar, P.M. Sarun, D. Kumar, Effect of $BaTiO_3$ addition on the microwave dielectric properties of MgO–Al_2O_3–SiO_2–TiO_2 glass-ceramic, Mater. Chem. Phys. 275 (2022) 125276, https://doi.org/10.1016/j.matchemphys.2021.125276.
[13] N.J. Lóh, L. Simão, C.A. Faller, A. De Noni, O.R.K. Montedo, A review of two-step sintering for ceramics, Ceram. Int. 42 (2016) 12556–12572, https://doi.org/10.1016/j.ceramint.2016.05.065.
[14] C. Xu, Z. Zhang, J. Zhang, L. Lei, D. Zhang, Z. Fu, A new route to fabricate barium titanate with high permittivity, Ceram. Int. 40 (2014) 10927–10931, https://doi.org/10.1016/j.ceramint.2014.03.090.

[15] S.A. Rasaki, D. Xiong, S. Xiong, F. Su, M. Idrees, Z. Chen, Photopolymerization-based additive manufacturing of ceramics: a systematic review, J. Adv. Ceram. 10 (2021) 442–471, https://doi.org/10.1007/s40145-021-0468-z.
[16] J. Guo, Y. Zeng, P. Li, J. Chen, Fine lattice structural titanium dioxide ceramic produced by DLP 3D printing, Ceram. Int. 45 (2019) 23007–23012, https://doi.org/10.1016/j.ceramint.2019.07.346.
[17] E. Stefan, T. Didriksen, T.O. Sunde, M.-L. Fontaine, H. Ræder, P.M. Rørvik, Effects of powder properties on the 3D printing of $BaTiO_3$ ceramic resins by stereolithography, Progr. Addit. Manuf. 8 (2023) 1641–1651, https://doi.org/10.1007/s40964-023-00431-w.
[18] S. Bhandari, G. Vajpayee, L.L. da Silva, M. Hinterstein, G. Franchin, P. Colombo, A review on additive manufacturing of piezoelectric ceramics: from feedstock development to properties of sintered parts, Mater. Sci. Eng. R Rep. 162 (2025) 100877, https://doi.org/10.1016/j.mser.2024.100877.
[19] S.P. Gentry, J.W. Halloran, Light scattering in absorbing ceramic suspensions: effect on the width and depth of photopolymerized features, J. Eur. Ceram. Soc. 35 (2015) 1895–1904, https://doi.org/10.1016/j.jeurceramsoc.2014.12.006.
[20] Z. Jiang, Y. Sun, J. Chen, Y. Zeng, Control of electromechanical performance in 3D printing lattice-structured $BaTiO_3$ piezoelectric ceramics, J. Adv. Ceram. 13 (2024) 987–1001, https://doi.org/10.26599/JAC.2024.9220912.
[21] K. Chen, Y. Wang, C. Wu, Y. Du, H. Tang, S. Zheng, Z. Zhou, H. Zheng, G. Wu, In vitro assessment of immunomodulatory and osteogenic properties in 3D-printed hydroxyapatite/barium titanate piezoelectric ceramic scaffolds, Ceram. Int. 50 (2024) 8751–8759, https://doi.org/10.1016/j.ceramint.2023.12.192.
[22] J. Cheng, Y. Chen, J.-W. Wu, X.-R. Ji, S.-H. Wu, 3D printing of $BaTiO_3$ piezoelectric ceramics for a focused ultrasonic array, Sensors 19 (2019) 4078, https://doi.org/10.3390/s19194078.
[23] A. Goulas, B. Ozkan, S. Saremi-Yarahmadi, B. Vaidhyanathan, Formulation-driven additive manufacturing of 3YSZ advanced ceramics via digital light processing, Open Ceram. 22 (2025) 100785, https://doi.org/10.1016/j.oceram.2025.100785.
[24] S. Chen, R. Wang, H. Li, H. Ye, J. Cheng, S. Wu, X. He, B. Jian, R. Tao, Q. Ge, High-precision $BaTiO_3$ piezoelectric ceramics via vat photopolymerization 3D printing, J. Eur. Ceram. Soc. 44 (2024) 116706, https://doi.org/10.1016/j.jeurceramsoc.2024.116706.
[25] C.-L. Liu, Q. Du, J.-M. Wu, G. Zhang, Y.-S. Shi, High piezoelectricity of 3D printed $BaTiO_3$–$xBaSnO_3$ piezoceramics via vat photopolymerization, J. Eur. Ceram. Soc. 44 (2024) 4639–4645, https://doi.org/10.1016/j.jeurceramsoc.2024.01.085.
[26] C. Long, Z. Liu, C. Liu, Z. Chen, Ceramic additive manufacturing via vat photopolymerization, Inside MS 4 (2025) 025200031, https://doi.org/10.36922/MSAM025200031.
[27] Y. Huan, X. Wang, J. Fang, L. Li, Grain size effect on piezoelectric and ferroelectric properties of $BaTiO_3$ ceramics, J. Eur. Ceram. Soc. 34 (2014) 1445–1448, https://doi.org/10.1016/j.jeurceramsoc.2013.11.030.
[28] R. Harizanova, S. Slavov, L. Vladislavova, L.C. Costa, G. Avdeev, C. Bocker, C. Rüssel, Barium titanate containing glass-ceramics—The effect of phase composition and microstructure on dielectric properties, Ceram. Int. 46 (2020) 24585–24591, https://doi.org/10.1016/j.ceramint.2020.06.247.
[29] M. Kuwabara, H. Matsuda, N. Kurata, E. Matsuyama, Shift of the curie point of barium titanate ceramics with sintering temperature, J. Am. Ceram. Soc. 80 (1997) 2590–2596, https://doi.org/10.1111/j.1151-2916.1997.tb03161.x.
[30] Y.-Z. Lin, K.H. Yang, H.-I. Hsiang, Effect of A/B ratio on the dielectric properties and insulation resistance of barium titanate sintered in a reducing atmosphere, Mater. Res. Bull. 178 (2024) 112877, https://doi.org/10.1016/j.materresbull.2024.112877.
[31] J. Lee, J. Jeong, J. Jung, H. Jeong, Optimizing dielectric constant in tetragonal $BaTiO_3$ via densification, tetragonality, and grain growth kinetic with sintering temperature, Arch. Metall. Mater. (2025) 765–769, https://doi.org/10.24425/amm.2025.153478.
[32] S.-M. Hwang, J.-C. Lim, S. Kim, J.-Y. Kim, J. Hwang, C. Lee, N. Kwon, I. Kim, K. Lee, S. Park, S.-M. Bae, J.-H. Hwang, K. Lee, H.-S. Kim, Impact of the change in charge compensation mechanism on the electrical, dielectric, and structural properties of La-doped $BaTiO_3$ ceramics, J. Eur. Ceram. Soc. 44 (2024) 5471–5479, https://doi.org/10.1016/j.jeurceramsoc.2023.12.029.
[33] J.C.C. Lin, W.-C.J. Wei, Low-temperature sintering of $BaTiO_3$ with Mn-Si-O glass, J. Electroceram. 25 (2010) 179–187, https://doi.org/10.1007/s10832-010-9613-8.
[34] Z. Sun, Y. Li, M. Liu, H. Jin, Y. Zhao, Screening of sintering aids for oxide ceramics: a case of NASICON electrolyte, Small 19 (2023) 2301230, https://doi.org/10.1002/smll.202301230.
[35] C. Liu, J. Zou, X. Wang, T. Zhang, G. Ye, T. Button, J. Binner, Processing, microstructure and piezoelectric properties of Li-doped BCZT ceramics, Ceram. Int. 49 (2023) 4119–4128, https://doi.org/10.1016/j.ceramint.2022.09.292.
[36] C.-L. Liu, Q. Du, C. Zhang, J.-M. Wu, G. Zhang, Y.-S. Shi, Fabrication and properties of $BaTiO_3$ ceramics via digital light processing for piezoelectric energy harvesters, Addit. Manuf. 56 (2022) 102940, https://doi.org/10.1016/j.addma.2022.102940.
[37] A. Smirnov, S. Chugunov, A. Kholodkova, M. Isachenkov, A. Tikhonov, O. Dubinin, I. Shishkovsky, The fabrication and characterization of $BaTiO_3$ piezoceramics using SLA 3D printing at 465 nm wavelength, Materials 15 (2022) 960, https://doi.org/10.3390/ma15030960.
[38] Y. Slimani, A. Selmi, E. Hannachi, M.A. Almessiere, G. AlFalah, L.F. AlOusi, G. Yasin, M. Iqbal, Study on the addition of SiO_2 nanowires to $BaTiO_3$: structure, morphology, electrical and dielectric properties, J. Phys. Chem. Solid. 156 (2021) 110183, https://doi.org/10.1016/j.jpcs.2021.110183.
[39] Y. Xiao, S. Yang, M. Wang, Y. Wang, T. Li, C. Li, J. Li, F. Li, Textured piezoelectric ceramics with reduced grain size for high-frequency transducer applications, Nat. Commun. 17 (2026) 3750, https://doi.org/10.1038/s41467-026-70360-z.
[40] L. Zhao, X. Yuan, X. Zhou, Q. Wang, J. Li, X. Xiong, Q. Zhang, C. Chen, S. Chen, D. Ju, Y. Zhang, D. Zhang, Three-dimensional honeycomb structured $BaTiO_3$-based piezoelectric ceramics via texturing and vat photopolymerization, Addit. Manuf. 95 (2024) 104542, https://doi.org/10.1016/j.addma.2024.104542.
[41] X. Zhao, Y. Sun, J. Chen, Y. Zeng, Highly HFOM three-dimensional anti-tetrachiral negative Poisson's ratio $BaTiO_3$ ceramics prepared via vat photopolymerization, Addit. Manuf. 109 (2025) 104872, https://doi.org/10.1016/j.addma.2025.104872.
[42] B. Jaffe, W.R. Cook Jr., H. Jaffe, Piezoelectric Ceramics, Academic Press, London, 1971.
[43] I. Fujii, S. Trolier-McKinstry, Temperature dependence of dielectric nonlinearity of $BaTiO_3$ ceramics, Microstructures 3 (2023) 2023045, https://doi.org/10.20517/microstructures.2023.43.
[44] W.J. Merz, The electric and optical behavior of $BaTiO_3$ single-domain crystals, Phys. Rev. 76 (1949) 1221–1225, https://doi.org/10.1103/PhysRev.76.1221.